ACS central science

Open Access

This article is licensed under CC-BY 4.0

http://pubs.acs.org/journal/acscii

Article

Two-Step Photon Absorption in an Expanded Perovskite Analog with a Molecular Intermediate Band

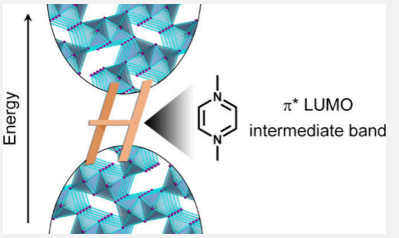
Zhiqiao Jiang, Kostas Fykouras,[†] Yorrick Boeije,[†] Kyle Frohna, Austin C. Flick, Garrett LeCroy, Syed Joy, Zhengkang Qu, Abigail Carbone, Julian A. Vigil, Akshay Rao, Alberto Salleo, Reinhold H. Dauskardt, Samuel D. Stranks, Kenneth R. Graham, Daniel N. Congreve, Linn Leppert,* and Hemamala I. Karunadasa*

Cite This: https://doi.org/10.1021/acscentsci.6c01379

Read Online

ACCESS | Metrics & More | Article Recommendations | Supporting Information

ABSTRACT: Intermediate-band solar cells (IBSCs) introduce an intermediate band (IB) within the absorber's band gap, allowing consecutive sub-band-gap two-step photon absorption (TSPA) to supplement band-gap absorption, enabling a 50% increase in the fundamental device efficiency limit. Current IBSC absorbers, however, introduce the IB as impurities in trace concentrations, affording weak sub-band-gap absorption. We demonstrate a novel material design for TSPA using $(dmpz)Pb_2I_6$ ($dmpz^{2+}$ = *N*,*N*′-dimethylpyrazinium) containing a *molecular* IB. Notably, the organic−inorganic hybridization evident in electronic structure calculations, where electronic states from the iodide appear in the dmpz-based bands, and large thermal fluctuations revealed by molecular dynamics trajectories enhance subgap absorption at 300 K. Transient electronic signatures of photoreduced $dmpz^{\bullet+}$ radicals verify the charge-transfer nature of the sub-band-gap absorption, whereas coherent high-frequency vibrations reveal vibronic coupling between dmpz and the inorganic framework. Proof-of-concept solar cells with $(dmpz)Pb_2I_6$ generate increased photocurrent upon subgap IR excitation and display quadratic-to-linear power dependence. This first demonstration of TSPA with an intrinsic organic IB offers a new material class for IBSCs.



1. INTRODUCTION

Tuning a solar-cell absorber's band gap to better match the energy range of the solar spectrum enables efficient harvesting of solar energy. But typical absorbers must compromise between absorbing more solar photons and producing a high solar-cell voltage. Wide-band-gap semiconductors absorb visible light and produce a high voltage in solar cells, but they waste the abundant sub-band-gap infrared (IR) photons (Figure 1A). Likewise, near-IR-band-gap materials effectively use a broader range of the solar spectrum, but waste higher-energy photons and produce low voltages in solar cells (Figure 1B).[1,2] An intriguing solution for harvesting IR photons, without compromising the voltage, is offered by the intermediate-band solar cell (IBSC). Here, an intermediate band (IB) is introduced between the filled valence band (VB) and empty conduction band (CB) of the absorber (Figure 1C).[3−7] With two-step photon absorption (TSPA), the VB → IB and IB → CB transitions augment the VB → CB band-gap transition. Thus, IBSCs can produce high current density while maintaining a high voltage. Theoretically, IBSCs can produce an efficiency of 48.9% under 1 sun illumination (AM 1.5G),[8] 1.5 times that of the detailed balance limit for single-junction solar cells (with one absorber)[1] and slightly higher than for double-junction solar cells (with two absorbers; 46%),[9] potentially with much simpler and cheaper device construction.

Current IBSC absorbers typically use inorganic semiconductors, introducing the IB through doping with transition metals,[10,11] main group elements,[12,13] or quantum dots.[14−19] However, along with defect-induced carrier recombination, increased carrier scattering, and lattice mismatch/strain, these methods introduce the IB only at trace concentrations,[7,20] limiting the absorption strength of optical transitions involving the IB.[21] Thus, to our knowledge, even among the highest-performing solar cells incorporating IB materials, such as a GaAs cell embedded with InAs quantum dots,[22] the measured efficiencies have remained below the theoretical predictions for ideal IBSCs, operating at similar efficiency and lower voltage than its counterpart without an IB.[23]

Organic IBSCs offer a different pathway for TSPA, through coupled singlet−triplet conversion, triplet−triplet annihilation, and upconversion;[24−27] however, the intrinsically low yield of some of these processes and the thermal instability of the molecules greatly limit efficiency and lifetime.[28,29]

This motivates the exploration of an entirely different materials class for TSPA. Here, we introduce a new design for

Received: August 10, 2026
Revised: October 19, 2026
Accepted: October 23, 2026

ACS Publications

© XXXX The Authors. Published by American Chemical Society

Downloaded from pubs.acs.org/acscii/article-pdf/doi/10.1021/acscentsci.6c01379/6918706/acscentsci.6c01379.pdf by STANFORD UNIV user on 13 November 2026

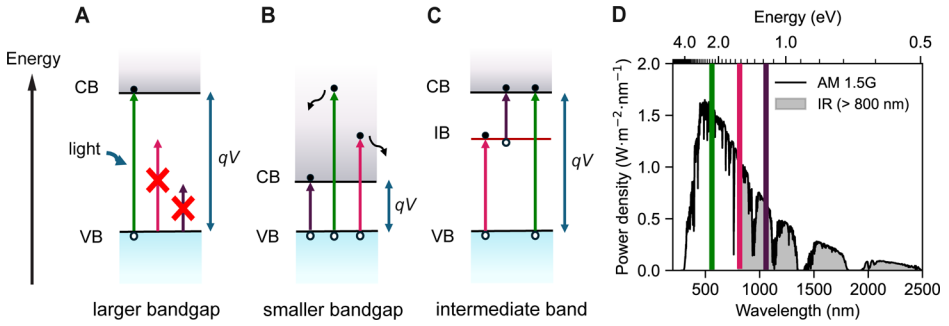


Figure 1. Energy-level diagrams of (A) a larger-band-gap solar absorber that cannot absorb IR photons (pink/brown arrows) but can produce a high voltage (V; highest obtainable voltage, blue double-headed arrow, where q is the elementary charge of an electron), (B) a smaller-band-gap absorber that can absorb IR photons but can produce only a low voltage, and (C) an IB absorber that can absorb IR photons and produce a high voltage. VB = valence band, IB = intermediate band, and CB = conduction band. (D) Standard solar spectrum (AM 1.5G, 1 sun; yearly average for mid-latitude regions)[86] with representative energies of the three photons (green, pink, and brown) shown in parts A–C. The shaded area corresponds to IR photons with >800 nm wavelengths.

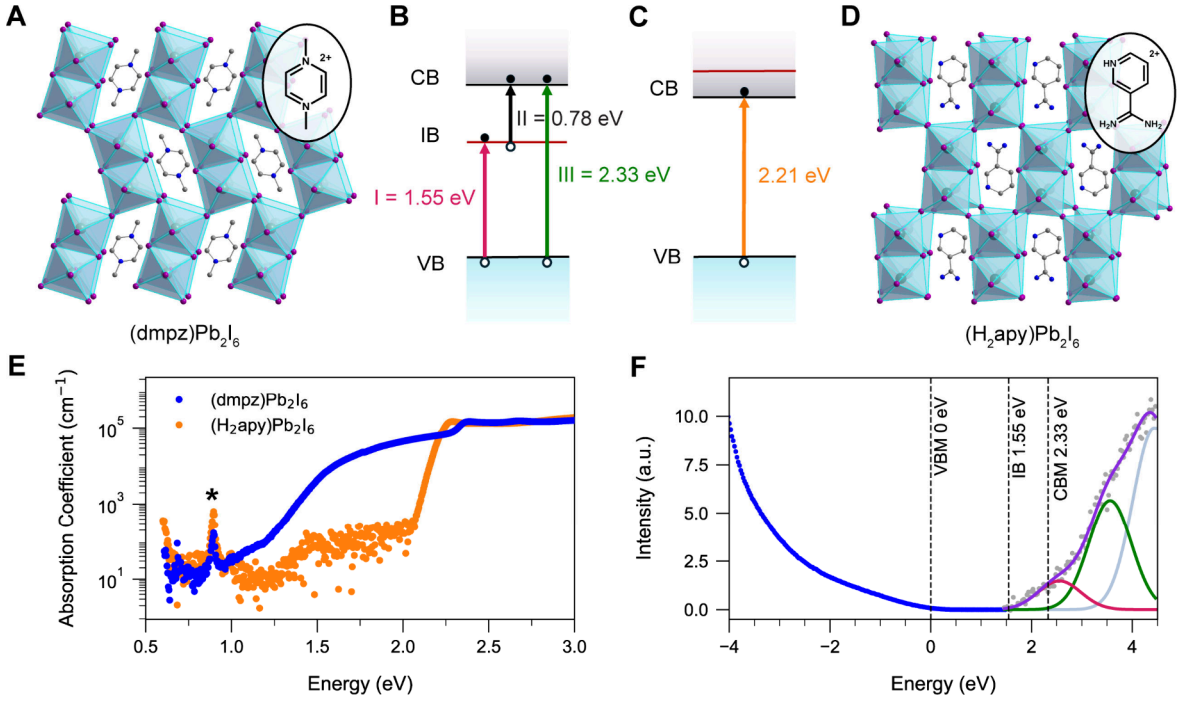


Figure 2. Single-crystal X-ray diffraction (SCXRD) structure (A) and schematic band diagram (B) of $(dmpz)Pb_2I_6$. SCXRD structure (D) and schematic band diagram (C) of $(H_2apy)Pb_2I_6$. Insets show the organic molecules in more detail. Figure 2A was adapted with permission from ref 30. Copyright 2020 John Wiley and Sons. The band energies are extracted from UPS and IPES measurements for $(dmpz)Pb_2I_6$ and from the UV–vis absorption onset for $(H_2apy)Pb_2I_6$. Dark red lines represent the energy of (B) $dmpz^{2+}$ and (C) H_2apy^{2+} molecular bands. (E) Combined PDS and UV–vis absorption spectra of $(dmpz)Pb_2I_6$ and $(H_2apy)Pb_2I_6$ thin films (see the Supporting Information). The peak marked by an asterisk at ~0.9 eV is from the fused silica (UV grade) substrates.[87] (F) UPS (left) and IPES (right) spectra of representative films of $(dmpz)Pb_2I_6$. The energy is shifted to align the VBM at 0 eV. For the UPS spectrum, the dark blue dots are experimental data. For the IPES spectrum, gray dots are the experimental data; the purple line is the value fitted from a three-term Gaussian function; the red, green, and light blue curves are the individual Gaussian functions, respectively.

an IBSC absorber, using organic molecules to form an IB within the band gap of a 3D inorganic semiconductor. For this, we demonstrate TSPA in $(dmpz)Pb_2I_6$ (dmpz = *N*,*N*′-dimethylpyrazinium), an expanded perovskite analogue.[30] Here, following the principles of cluster expansion in framework materials,[31] the PbX_6 octahedra in the $APbX_3$ 3D perovskites (A = monovalent cation; X = halide) are replaced by Pb_2X_{10} dimers of edge-sharing octahedra, which share corners to maintain the 3D connectivity of the parent framework. These expanded frameworks have larger A-site cavities,[30,32,33] which can accommodate divalent aromatic molecules. In particular, $(dmpz)Pb_2I_6$ exhibits a unique band structure stemming from the low-lying π^* orbitals of $dmpz^{2+}$ that form an empty IB within the band gap of the Pb–I framework (Figure 2A,B). Importantly, unlike lower-dimensional hybrid materials with conjugated organic molecules, the expanded perovskite analogues maintain 3D inorganic band dispersion, enabling more isotropic electronic conductivity.[34−36] To our knowledge, this is the first inorganic semiconductor to achieve TSPA with an intrinsic IB acceptor, without extrinsic additives/dopants.

https://doi.org/10.1021/acscentsci.6c01379
ACS Cent. Sci. XXXX, XXX, XXX−XXX

Downloaded from pubs.acs.org/acscii/article-pdf/doi/10.1021/acscentsci.6c01379/6918706/acscentsci.6c01379.pdf by STANFORD UNIV user on 13 November 2026

2. RESULTS AND DISCUSSION

2.1. The Intermediate Band in (dmpz)Pb_2I_6

We synthesized (dmpz)Pb_2I_6 (Figure 2A) as previously reported.[30] To isolate the effects of the IB, we also synthesized an analog without the IB: (H_2apy)Pb_2I_6 (H_2apy = *N*,*N*′-dihydro-3-amidinopyridinium; see the Supporting Information; Figure 2D). Its Sn analog, (H_2apy)Sn_2I_6, was recently reported.[37] Photothermal deflection spectroscopy (PDS) data show that (H_2apy)Pb_2I_6 starts absorbing light only near its valence band maximum (VBM) → conduction band minimum (CBM) band-edge transition at 2.21 eV, whereas (dmpz)Pb_2I_6 clearly shows a sub-band-gap absorption onset at 1.47 eV, below the VBM → CBM transition onset at 2.27 eV (Figures 2E and S9). Notably, the sub-band-gap transitions in (dmpz)Pb_2I_6 have high absorption coefficients (10^3 to 10^5 cm^{-1}). Ultraviolet photoelectron spectroscopy (UPS) measurements place the VB−IB energy gap at 1.55 eV, whereas inverse photoemission spectroscopy (IPES) measurements place the VBM−CBM energy gap at 2.33 eV. These energy gaps match the features of the fitted optical absorption spectrum (Figures 2F and S9).

2.2. Band Structure and Molecular Dynamics (MD) at 300 K

We previously reported the band structure of (dmpz)Pb_2I_6[30] and (dmpz)Sn_2I_6,[38] highlighting the dmpz-based band within the band gap. This band structure was recently revisited in a computational study on two-step photon absorbers,[39] although as we show here, their static, 0-K-band structure from standard DFT calculations does not capture the features that allow (dmpz)Pb_2I_6 to act as a two-step photon absorber.

Here, we calculate the electronic band structures of (dmpz)Pb_2I_6 and (H_2apy)Pb_2I_6 using the first-principles *GW* approach,[40] using the Quantum Espresso simulation package[41,42] for DFT and the BerkeleyGW package[43,44] for *GW* calculations (see the Supporting Information). Our band-structure calculations corroborate the IB in (dmpz)Pb_2I_6 dominated by $dmpz^{2+}$ molecular orbitals (Figure 3A).[30,38] Using the G_0W_0@PBE method, including spin−orbit coupling (SOC) self-consistently, the VBM−IB energy gap is 1.4 eV, close to the experimental value of 1.55 eV. The IB originates from the LUMOs (lowest unoccupied molecular orbitals) of two nonequivalent $dmpz^{2+}$ molecules in the unit cell, denoted LUMO and LUMO′, with a ∼10% contribution from I 5p orbitals. This hybridization with the inorganic framework gives the IB a significant dispersion, not expected from a purely molecular (0D) band. Such hybridization is crucial for TSPA: zero hybridization precludes transitions between an organic-based IB and inorganic-based VB and CB, whereas excessive hybridization should drive rapid CB → IB or IB → VB recombination, which are nonradiative recombination pathways that should reduce current extraction efficiency and cell voltage. The $dmpz^{2+}$ LUMO+1 bands lie above the inorganic CBM.

Both the VB and CB in (dmpz)Pb_2I_6 are dispersive, forming a direct band gap at *Z*. The VBM is derived from I 5p and Pb 6s orbitals and the CBM is derived from Pb 6p and I 5p, as in typical lead-iodide perovskites. Our G_0W_0 calculations underestimate the VBM → CBM transition, as seen in lead-halide perovskites.[45,46] We therefore rigidly shifted all CBs to be 0.6 eV above the IB, to match experimental UPS/IPES data of (dmpz)Pb_2I_6 (see Supplementary Note 1). In contrast, the electronic band structure of (H_2apy)Pb_2I_6 has no IB; both the H_2apy LUMO and the LUMO+1 bands are located above the CBM (Figure 3B).

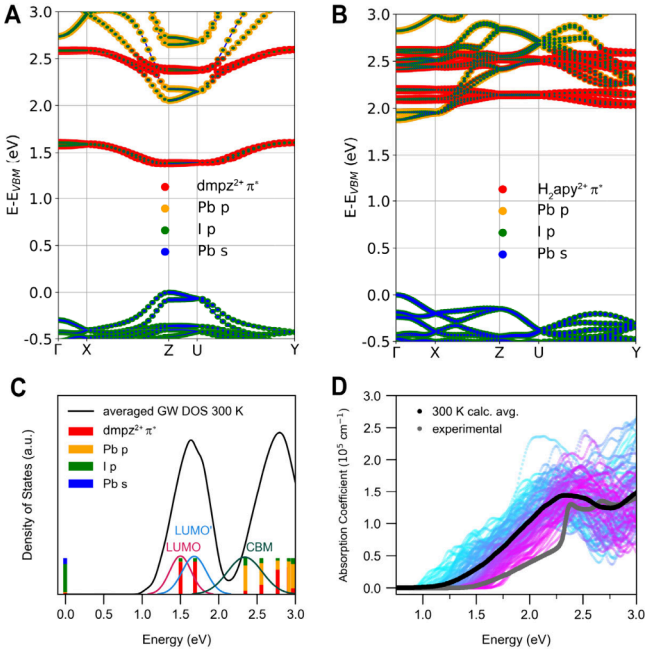


Figure 3. DFT-PBE+SOC band structures of (A) (dmpz)Pb_2I_6 and (B) (H_2apy)Pb_2I_6 at 0 K. All conduction and intermediate bands are rigidly shifted to match the G_0W_0@PBE+SOC band gap. For (dmpz)Pb_2I_6, all conduction bands are further shifted to match the experimental IB → CBM energy gap (+0.6 eV). Orbital contributions are shown in color, with red, orange, green, and blue representing $dmpz^{2+}$ π* LUMOs, Pb 6p, I 5p, and Pb 6s orbitals, respectively. (C) *GW*@PBE+SOC DOS averaged over 100 MD snapshots at 300 K (black line). The *x*-axis values of vertical bars represent the averaged band energy at the high-symmetry *Z* point, whereas the colors correspond to the orbital composition of the band. Gaussian functions over the vertical bars represent the distribution of the *Z*-point energy of the specific band across 100 MD snapshots. (D) Linear optical absorption spectrum calculated with the *GW*+BSE method over 100 MD snapshots at 300 K (blue to pink colored lines), the average of 100 calculated spectra (black line), and the experimental optical absorption spectrum at 300 K (gray line).

To explore how thermal fluctuations affected the electronic structure and absorption spectrum of (dmpz)Pb_2I_6, we performed MD simulations using interatomic machine-learned force fields (MLFF) as implemented in VASP (see the Supporting Information). After 2 ps of equilibration at 300 K, an 8 ps trajectory was collected. From the last ps, 100 structure snapshots were extracted at 10 fs intervals (Supplementary Video 1 and Supplementary Video 2). We then calculated band structures (Supplementary Video 3), density of states (DOS), and absorption spectra of these snapshots with the G_0W_0@PBE +BSE approach. The vertical bars in the DOS calculations (Figure 3C) give the average energy of the LUMO, LUMO′, and CBM at the *Z* point; the width of the Gaussians corresponds to the standard deviation of this average. At 300 K, the *GW* DOS reveal a 1.50 eV VBM−IB energy gap and a 2.35 eV VBM−CBM band gap, closely agreeing with the experimental values of 1.55 and 2.33 eV from IPES/UPS spectra, respectively (Figure 2F). Thermal fluctuations broaden these transition energies (Figure S10), with the VB → IB transition onset redshifting to ∼1.1 eV and the VB → CB transition onset redshifting to ∼1.7 eV (Figure 3C). Indeed, as shown later, photoexcitation at 1.27 and 1.95 eV can partially drive VB electrons to the IB and to the CB, respectively.

Downloaded from pubs.acs.org/acscii/article-pdf/doi/10.1021/acscentsci.6c01379/6918706/acscentsci.6c01379.pdf by STANFORD UNIV user on 13 November 2026

https://doi.org/10.1021/acscentsci.6c01379
ACS Cent. Sci. XXXX, XXX, XXX−XXX

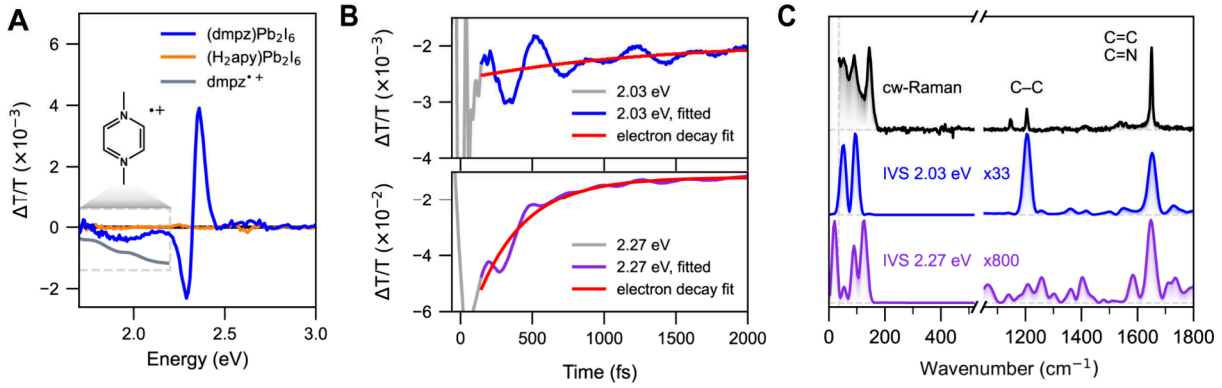


Figure 4. TA spectra of (A) $(dmpz)Pb_2I_6$ and $(H_2apy)Pb_2I_6$ thin films, integrated between 1 and 3 ps, photoexcited at 2.03 eV. A fluence of 42.0 $\mu J/cm^2$ was used for $(dmpz)Pb_2I_6$ and 211 $\mu J/cm^2$ for $(H_2apy)Pb_2I_6$. Inset: Close-up showing the scaled absorption spectrum of $dmpz^{\bullet+}$ radicals in acetonitrile overlaid in gray; see Figure S15 for the full spectrum. (B) IVS of $(dmpz)Pb_2I_6$ integrated at 2.02−2.05 eV (top) and 2.25−2.30 eV (bottom). The electronic decay is removed through biexponential fitting. The gray temporal region is excluded from the fit to remove coherent artifacts arising from the pump−probe interaction. (C) FFT spectra of IVS (blue and purple traces) and the continuous-wave (cw) Raman spectrum of $(dmpz)Pb_2I_6$ (black trace). Frequencies below ~30 cm^{-1} should be interpreted with caution because the finite temporal measurement window limits the frequency resolution in this region. Conversely, the corresponding low-frequency region is inaccessible in the cw Raman spectrum due to strong Rayleigh scattering. The high-frequency (>1000 cm^{-1}) regions of the FFT spectra are scaled to show details.

Although individual snapshots show sharp peaks with high oscillator strength in the calculated absorption spectra, averaging over 100 configurations produces a smooth absorption onset consistent with the experimental spectrum (Figure 3D). Calculated transition dipole matrix elements show that the VBM → CBM transitions have a significantly larger oscillator strength than the VBM → IB transitions (Figure S39), although the latter remains optically active due to the ~10% I 5p character of the IB. The IB → CB transition similarly has a still lower, but nonnegligible oscillator strength, providing a theoretical explanation for TSPA (Figure S40). The calculated absorption spectra with and without electron−hole interaction (Figure S12), indicate small exciton binding energy, beneficial for photocurrent extraction.

2.3. Characterizing the Photoexcited State

We used transient absorption (TA) spectroscopy to investigate the excited-state dynamics; numerous studies have investigated charge transfer between the inorganic and organic components of 2D lead-halide perovskites using this method.[47,48] Here, excitation at a selected energy is followed by a broadband probe of the excited state. Photoexcitation of $(dmpz)Pb_2I_6$ at 2.03 eV mainly targets the VB → IB transition and leads to a strong ground-state bleach at 2.38 eV (Figure 4A)—close to the VBM → CBM band-gap transition—indicating a decrease in the valence-band electron population.[49] A below-band-gap sharp photoinduced absorption at 2.34 eV produces a derivative-like spectral feature, which is attributed to band-gap renormalization resulting from Coulomb screening, as seen in related materials.[50,51]

A broad photoinduced absorption appears at 1.8−2.1 eV (Figures 4A and S17A),[52,53] which is assigned to an intramolecular transition within the photogenerated radical $dmpz^{\bullet+}$ (dmpz LUMO → LUMO+1). Indeed, chemically generated $dmpz^{\bullet+}$ is a stable species, and its absorption spectrum has a peak at a similar energy to this TA feature (Figures 4A inset, and S15). The ground-state bleach (consistent with depleting electrons from the VBM) and the photoinduced absorption (consistent with $dmpz^{2+}$ reduction to $dmpz^{\bullet+}$) indicate that the 2.03 eV excitation drives a Pb−I framework → dmpz charge-transfer transition, underscoring the organic−inorganic hybridization revealed in our calculations.

The magnitude of the photoinduced absorption at 1.8−2.1 eV reflects the IB electron population. When normalized against carrier density, this signal magnitude is similar for both 2.03 eV (below band gap, mainly VB → IB) and 3.10 eV (above band gap, VB → CB) excitations (Figure S16), indicating that $dmpz^{\bullet+}$ is formed through both direct VB → IB excitation as well as CB → IB electron decay (further discussed in Section 4). In contrast, neither sub-band-gap 2.03 eV excitation (Figures 4A and S17B) nor above-band-gap excitation at 2.48 and 3.10 eV (Figure S18) produces a transient response at 1.8−2.1 eV for $(H_2apy)Pb_2I_6$, consistent with the lack of an IB and corroborating its origin from photoreduced $dmpz^{\bullet+}$. The photoexcited-state recombination kinetics are discussed in the Supporting Information.

We then performed impulsive vibrational spectroscopy (IVS), where $(dmpz)Pb_2I_6$ is excited with an ultrashort (~13 fs) pump pulse from 1.4−1.9 eV and centered at 1.75 eV, which coherently excites vibrational modes. To investigate what vibrations are coupled to the charge-transfer absorption edge, we tracked the impulsively excited vibrations with a broadband probe (Figure S19). The optical response is converted into frequency space through fast Fourier transform (FFT) after subtracting the population decay (Figure 4C), yielding predominant low-frequency vibrations (<150 cm^{-1}) assigned to inorganic-framework vibrations (Figure S14).[54−56] Nevertheless, with the probe energy integrated within the range of the photoinduced absorption assigned to $dmpz^{\bullet+}$ (2.02−2.05 eV; Figure 4A), high-frequency modes at 1205 and 1653 cm^{-1} appear, which are assigned to the C−N and C═N/C═C stretches, respectively. These peaks diminish when the probe energy falls out of the photoinduced absorption region (2.25−2.30 eV; Figures 4C and S20). The real-time observation of molecular vibrations coupled to the VB → IB transition verifies its charge-transfer nature and reveals sufficient hybridization for vibronic coupling between dmpz and the inorganic framework. Such coherent modulation of electronic states by molecular vibrations is unusual in perovskites, where the electronic transitions are restricted to the inorganic framework. Thus, whereas the 300-K calculated absorption spectrum displays a

Downloaded from pubs.acs.org/acscii/article-pdf/doi/10.1021/acscentsci.6c01379/6918706/acscentsci.6c01379.pdf by STANFORD UNIV user on 13 November 2026

https://doi.org/10.1021/acscentsci.6c01379
ACS Cent. Sci. XXXX, XXX, XXX−XXX

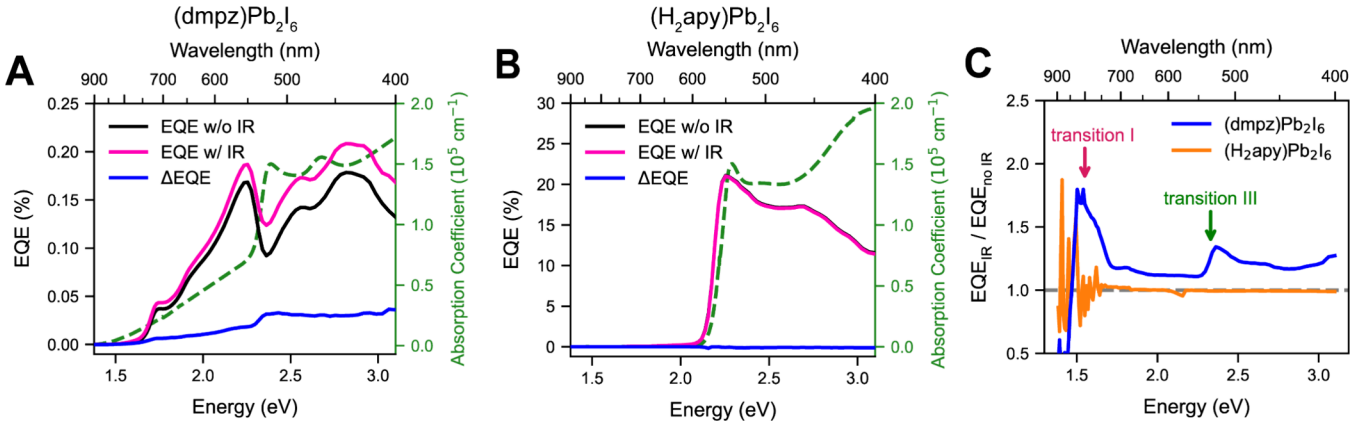


Figure 5. EQE for a solar cell without additional IR bias light (black), EQE with additional IR bias light (pink), and the difference between the EQE with and without the IR bias light (ΔEQE; blue), and PDS spectra (green) of thin films, for (A) $(dmpz)Pb_2I_6$ and (B) $(H_2apy)Pb_2I_6$. (C) Change in the EQE due to the IR light given as the ratio of EQE with IR (EQE_{IR}) over EQE without IR ($EQE_{no\ IR}$) for devices with $(dmpz)Pb_2I_6$ and $(H_2apy)Pb_2I_6$. The energy of the IR bias light is 1.27 eV (980 nm). Arrows at 1.55 eV (pink) and 2.33 eV (green) correspond to the energies of the VBM → IB (I) and VBM → CBM (III) transitions, respectively. Transitions I and III are labeled in Figure 2B.

vibrationally broadened absorption edge, density functional perturbation theory calculations identify the molecular vibrational eigenvectors that couple to this transition (Figure S14).

2.4. Confirming Two-Step Photon Absorption (TSPA)

We then fabricated a proof-of-concept intermediate-band solar cell (IBSC) with a $(dmpz)Pb_2I_6$ absorber. The insolubility of $(dmpz)Pb_2I_6$ is a distinct advantage for applications,[30] but it makes film deposition from solution challenging. So we modified the previously developed two-step deposition process for films.[30] First a $(CH_3NH_3)PbI_3$ film was evaporated on to the substrate, then a solution of $(dmpz)(BF_4)_2$ was cast over the $(CH_3NH_3)PbI_3$ film, converting it into $(dmpz)Pb_2I_6$ (see the Supporting Information). Infrared spectroscopy and thin-film diffraction measurements confirmed that no $(CH_3NH_3)PbI_3$ remained after conversion (Figures S6 and S22). Although typical 3D lead-iodide perovskites are unstable to humidity,[57,58] $(dmpz)Pb_2I_6$ thin films are stable for over a year in dry air in the dark, and for over a month in approximately 76% humidity (Figures S6 and S23).

Both $(dmpz)Pb_2I_6$ and $(H_2apy)Pb_2I_6$ were fabricated into solar cells with an inverted architecture (Figure S25A) with nickel oxide as the hole transport layer and PCBM ([6,6]-phenyl-C_{61}-butyric acid methyl ester) as the electron transport layer. IBSCs require efficient charge extraction from the CB. In $(dmpz)Pb_2I_6$-based devices, the IB is not highly dispersive (due to the mostly molecular character of the band), so carrier extraction from the IB is not as likely as from the CB. Nevertheless, PCBM was specifically chosen as the electron transport layer to impede direct electron extraction from the IB as the CB energy of PCBM is close to that of $(dmpz)Pb_2I_6$ (Figure S25B) and well above the IB.

In the external quantum efficiency (EQE) spectra, $(dmpz)Pb_2I_6$ shows a significant intensity in the 1.65−2.25 eV region (black curves, Figures 5A and S30C), which is above the VB → IB transition but below the VB → CB band-gap transition, as confirmed by the energy levels obtained from photothermal deflection spectra (green curve, Figures 5A and S30C). This clear sub-band-gap photocurrent is attributed to TSPA[14] due to the strong sub-band-gap absorption of $(dmpz)Pb_2I_6$. In contrast, $(H_2apy)Pb_2I_6$ behaves as a typical semiconductor without an IB, lacking pronounced sub-band-gap absorption and with a photocurrent onset matching the VBM → CBM band-gap onset (Figure 5B). The small photocurrent below the band gap (1.65−2.07 eV) is likely due to shallow defects.[59,60]

To confirm TSPA in $(dmpz)Pb_2I_6$, we then performed two-photon sub-band-gap photocurrent measurements (Figure S28). With the primary monochromatic light source varying from 1.38 to 3.10 eV, an IR bias light of 1.27 eV (980 nm) was applied. The IR bias light primarily drives the IB → CB transition, but it also catches the tail of the VB → IB transition due to the thermal fluctuations discussed in Section 2. Since the ΔEQE spectra measure the increase in photocurrent due to the IR bias (exciting IB electrons to the CBM), the intensity should increase only when the energy of the primary-source photons exceeds the VBM → IB transition threshold. As expected, $(dmpz)Pb_2I_6$ devices show a clear increase in ΔEQE under the IR bias with an onset of 1.50 eV, which is around the VBM → IB transition energy of 1.55 eV (blue curves, Figures 5A and S30C). The devices were measured four times in immediate succession: once with the IR bias off, twice with the IR bias on, and once more with the IR bias off. The two IR-off scans show similar photocurrent, and the two IR-on scans are similarly consistent (Figures S30A,B and 31). Such reproducibility suggests that the measurements are stable and that cumulative thermal effects from IR illumination are not major contributors to the ΔEQE values. Furthermore, the ΔEQE increases when the primary-source photon energy is around the VBM → CBM transition (~2.33 eV) and then plateaus at higher energy. This ΔEQE increase indicates that some CB electrons decay to the IB and are then excited back into the CBM by the IR bias light. Such CBM → IB back electron transfer is also evident in our TA measurements (Figures S16 and S18) and in other IBSCs.[19] The higher ΔEQE intensity above the VBM → CBM transition (>2.32 eV), compared to the region between the VBM → CBM and the VBM → IB transitions (1.77−2.25 eV) can be attributed to the higher absorption coefficient for the VBM → CBM transition. In contrast, $(H_2apy)Pb_2I_6$, with no IB, shows no significant change in ΔEQE intensity with the IR bias (Figure 5B; see Figure S30C,D for the logarithmic plots of Figure 5A,B).

The $(H_2apy)Pb_2I_6$-based devices have a substantially higher photocurrent compared to that from $(dmpz)Pb_2I_6$-based devices, which may be attributed to greater octahedral tilting (which should decrease band dispersion and carrier mobility), and lower film quality (due to the different film deposition

Downloaded from pubs.acs.org/acscii/article-pdf/doi/10.1021/acscentsci.6c01379/6918706/acscentsci.6c01379.pdf by STANFORD UNIV user on 13 November 2026

https://doi.org/10.1021/acscentsci.6c01379
ACS Cent. Sci. XXXX, XXX, XXX−XXX

method required) in the latter, as discussed in the Supporting Information Note 6. To compare two materials with different conductivity, we use the intensity ratio of EQE with IR over EQE without IR (Figure 5C). At energies above the low-energy noise region, this ratio remains constant at 1 for $(H_2apy)Pb_2I_6$, indicating no response to the IR bias. For $(dmpz)Pb_2I_6$, however, the ratio increases and peaks at a greater than 1 value around 1.5 eV as the excitation energy surpasses the VBM → IB transition, indicating IR-induced photocurrent from the IB → CB transition. The ratio reaches a second maximum (a greater than 1 value) around 2.3 eV, corresponding to the VBM → CBM transition energy, when the IR bias can re-excite electrons that decayed from the CB to IB, consistent with observations from EQE and ΔEQE data.

2.5. Power Dependence

Power-dependence measurements can further elucidate the nature of the absorption process involving the IB. For TSPA, before the IB saturates with carriers, the photocurrent should exhibit a quadratic dependence on the incident light intensity, which is proportional to carrier density.[61] Upon 1.27 eV excitation, the power dependence plot (log of photocurrent density vs log of incident power density) of a $(dmpz)Pb_2I_6$ solar cell changes in slope from 2.08 to 1.17 at a light intensity of ca. 0.473 mW/cm^2 (Figure 6). At lower light intensity, the

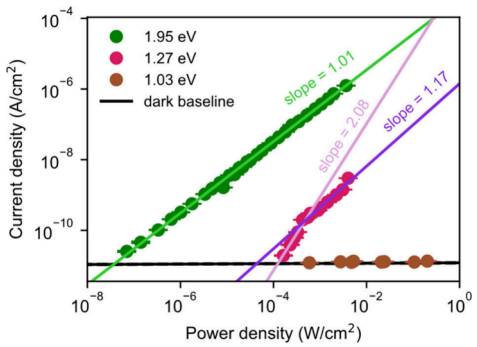


Figure 6. Power-dependence measurements of photocurrent of $(dmpz)Pb_2I_6$ devices with 1.95 eV (637 nm), 1.27 eV (980 nm), and 1.03 eV (1208 nm) excitations.

unsaturated IB carrier concentration depends on the light intensity, resulting in a quadratic relationship and a slope of 2 in the power dependence fit. At higher light intensity, however, a saturated IB carrier density no longer depends on light intensity, affording a slope of 1 in the logarithmic fit. Although 1.27 eV is below the 1.55 eV VBM → IB gap measured from UPS/IPES, the large thermal fluctuations of the IB and CB energies revealed in MD trajectories (Supplementary Video 1) and DOS calculations (Figure 3C) can reduce this VBM → IB gap to ca. 1.1 eV. Calculated absorption spectra of individual MD snapshots also indicate a range of absorption onsets with the lowest around 1 eV (Figure 3D), as also seen in the onset of the experimental absorption coefficients at ca. 1 eV (Figure 2E).

The 1.95 eV excitation can catch the low-energy tail of the VBM → CBM transition energy distribution (for a band gap of 2.33 eV) due to the previously mentioned thermal fluctuations of the bands seen in the MD simulations (Figure 3C), enabling one-step transitions resulting in a linear power dependence (Figure 6). Simplified modeling of the IBSC (Supporting Information) reveals that although the 1.95 eV excitation can catch the higher-energy tail of the VBM → IB process, the VB → CB transition dominates the overall photocurrent generation with its higher absorption coefficient (Figure S44D). In comparison, IR excitation at 1.03 eV does not produce photocurrent, since the energy is smaller than the VBM → IB transition, even considering 300-K thermal fluctuations. Further, neither 1.03 eV nor 1.27 eV excitation produces photocurrent in $(H_2apy)Pb_2I_6$ devices under similar conditions, since the excitation energies are much smaller than the absorber band gap of 2.21 eV (Figure S9A). The 1.95 eV excitation produces a linear power-dependence of the photocurrent for $(H_2apy)Pb_2I_6$ solar cells, indicating a one-photon process, likely involving shallow defects near the band gap[59,60] (Figure S33).

3. CONCLUSION

We have demonstrated the first example, to our knowledge, of a two-step photon absorber (TSPA) using stoichiometric acceptor states from organic molecules to form the IB within an inorganic semiconductor. We show that organic−inorganic orbital hybridization in the IB of $(dmpz)Pb_2I_6$ is crucial for maintaining the delicate balance between allowing sub-band-gap absorption and preventing rapid recombination, enabling sequential VB → IB → CB charge transfer.

First-principles calculations based on 300-K MD trajectories identify large thermal fluctuations of the IB and CB as the microscopic origin of the gradual increase in absorption coefficients, observed in both the calculated and experimental absorption spectra. TA and IVS measurements further elucidate the coupling between inorganic and organic components by identifying the formation of photoreduced $dmpz^{\bullet+}$ radicals, indicating VB → IB and CB → IB electron transfer, and the subsequent coupling of molecular vibrations to this charge-transfer state.

EQE and ΔEQE measurements of $(dmpz)Pb_2I_6$-based devices show increased photocurrent when a 1.27 eV IR bias excitation is applied, revealing that the IB → CB transition generates photocurrent. Our devices were designed for electron extraction from the CB of $(dmpz)Pb_2I_6$, with an electron transport layer whose acceptor level is energetically aligned with the $(dmpz)Pb_2I_6$ CB and well above its IB (Figure S25B). Further, the molecular IB is not highly dispersive, so carrier extraction from the IB is not as likely as from the CB. The repeated, consecutive measurements of the photocurrent with and without the IR bias light also suggest that thermal effects to the ΔEQE are negligible. Therefore, these ΔEQE measurements indicate an IBSC. Further, power-dependence measurements at 1.27 eV excitation reveal a transition from quadratic to linear behavior, further confirming TSPA, saturating at a power density of 0.473 mW/cm^2 (see the Supporting Information for modeling).

Our proof-of-concept $(dmpz)Pb_2I_6$ devices demonstrate TSPA with an organic IB. The poor metrics in the unoptimized devices (Figure S27) call for further improvements in the contact layers and interfacial recombination pathways to mitigate nonradiative decay and low electronic conductivity to reach the theoretically predicted voltages and efficiencies. TSPA and ΔEQE in many IBSCs are measured only at low temperatures (4−36 K)[14,16−18] due to the small IB−CB energy separation (~0.5 eV) in the absorbers, and the rapid IB ↔ CB thermal excitation/relaxation of carriers that precludes room-temperature characterization.[21] In contrast, the $(dmpz)Pb_2I_6$-based IBSCs operate at ambient conditions and 1 sun (Figure S29), stemming from moderate coupling between the IB and VB/CB.

Downloaded from pubs.acs.org/acscii/article-pdf/doi/10.1021/acscentsci.6c01379/6918706/acscentsci.6c01379.pdf by STANFORD UNIV user on 13 November 2026

https://doi.org/10.1021/acscentsci.6c01379
ACS Cent. Sci. XXXX, XXX, XXX−XXX

Importantly, this IBSC design can now be extended to other semiconductors with stoichiometric molecular acceptors. Here we outline the important considerations for this new TSPA: moderate organic−inorganic hybridization, thermal fluctuations that substantially modify the optical transition energies, and the photostability of the photoexcited organic radical. Compared to traditional IBSC absorbers, the hybrid absorbers presented here offer entirely different routes for optimization, potentially with greater tunability of the intermediate band energy, hybridization, and absorption cross section.

4. METHODS

4.1. General Procedures and Methods

All manipulations were performed in air unless otherwise noted. The solvents dimethylformamide (DMF), methanol (MeOH), and dichloromethane (DCM) were dried and degassed using a JC Meyer solvent purification system. Solid *N*,*N*′-dimethylpyrazinium tetrafluoroborate [dmpz$(BF_4)_2$] was synthesized with modifications to a previous report.[30] All other reagents were purchased from commercial sources and used without further purification. Abbreviations used: MA = methylammonium, dmpz = *N*,*N*′-dimethylpyrazinium, H_2apy = 3-amidinopyridinium, PCBM = phenyl-C61-butyric acid methyl ester, BCP = bathocuproine, ITO = indium tin oxide. C, H, N elemental analysis was performed under air-free conditions by Midwest Microlab (Indianapolis, IN). All C, H, N analyses are reported as the average of duplicate measurements.

4.2. Substrate Preparation

Substrates (glass for UV−visible spectroscopy measurements and powder X-ray diffraction measurements, ITO (180 ± 25 nm) on glass for SEM and device fabrication; all 2 cm × 2 cm in size) were scrubbed then sonicated in detergent, deionized water, acetone, and isopropanol, sequentially for 10 min each. The substrates were then blow-dried with compressed air and treated with UV-ozone cleaner for 15 min prior to film deposition.

4.3. Deposition of (MA)PbI_3 Thin Films

Films of (MA)PbI_3 were deposited on substrates through two-step sequential thermal evaporation, modified from a previous report.[62] Clean substrates were brought into a nitrogen-filled glovebox and mounted on the substrate holder of a custom single-source thermal evaporator (Thermionics VE-90 vacuum system controller with Inficon XTM/2 deposition monitor). Powders of PbI_2 were mounted on a tantalum boat (Kurt J. Lesker) and connected to the electrical leads. The chamber was pumped down to ca. 5×10^{-6} Torr or lower before the source was heated. The PbI_2 layer was first deposited with a current of 6.3 A and at a rate of 0.7−0.9 Å/s until the thickness was 100 nm. The chamber was brought back to ambient pressure, and (MA)I powder was loaded using a different tantalum boat. The (MA)I layer was deposited with a current of 5.8 A and at a rate of 0.8−1.3 Å/s until the thickness reached 100 nm. The films were then annealed under a N_2 environment for 5 min at 100 °C.

4.4. Deposition of (dmpz)Pb_2I_6 Thin Films

Due to the insolubility of (dmpz)Pb_2I_6 in water, thin films of (dmpz)Pb_2I_6 were fabricated by converting (MA)PbI_3 thin films, by modifying a previous report.[30] The following procedure was performed under a N_2 environment. For each film to be converted, dmpz$(BF_4)_2$ powder (10 mg, 0.035 mmol) was dissolved in MeOH (630 μL) and stirred at room temperature. The solution was then immediately filtered and slowly drop-casted on the (MA)PbI_3 film that was spinning at 4500 rpm. The film was left spinning for 30 s after the dropcasting was completed and then annealed at 100 °C for 20 min.

4.5. Single Crystals and Powders of (H_2apy)Pb_2I_6

For single crystals, PbI_2 (500 mg, 1.08 mmol) and 3-aminopyridine hydrochloride (70 mg, 0.74 mmol) powders were dissolved in HI aq. (7.57 M, 2 mL) in a 4 mL vial. The solution was stirred at 100 °C as a red powder precipitated. After a quick hot filtration, the yellow filtrate was brought back to 100 °C and cooled down to room temperature at a rate of 5 °C/h. Red crystals formed at the bottom of the vial. For powders, a similar procedure was used, except for the hot filtration. As the supernatant turned yellow and a red precipitate formed, the solution was cooled to room temperature by turning off the heat source. The red precipitate was collected by filtration and rinsed with acetone. The powder was dried at reduced pressure overnight. Anal. Calc. for $C_6H_9N_3Pb_2I_6$: C, 5.55%; H, 0.70%; N, 3.24%. Found: C, 5.70%; H, 0.66%; N, 3.15%.

4.6. Deposition of (H_2apy)Pb_2I_6 Films

Under a N_2 environment, (H_2apy)Pb_2I_6 powder (91.0 mg, 0.07 mmol) was added to DMF (322.5 μL). The solution was stirred at 100 °C until complete dissolution was observed and then used immediately after filtration. The substrates were preheated at 100 °C for 10 min. Films were fabricated by spin-coating 60 μL of the solution on the hot substrate at 4500 rpm for 1 min. The films were annealed at 60 °C for 2 min then at 100 °C for 15 min.

4.7. Solar-Cell Device Fabrication

The perovskite solar-cell devices were fabricated in the following configuration: ITO/NiO_x/perovskite/(C_{60} or PCBM)/BCP/Ag. A thin layer of NiO_x (20 nm) was deposited on cleaned ITO/glass substrates through the sol−gel method. A solution of $Ni(NO_3)\cdot 6H_2O$ (0.8 M) was prepared by dissolving 697.9 mg $Ni(NO_3)\cdot 6H_2O$ in 3 mL of dry ethylene glycol and ethylenediamine (94:6 v/v). The cloudy solution was stirred in the glovebox overnight to produce a sapphire-blue clear solution. The $Ni(NO_3)\cdot 6H_2O$ solution was then brought out of the glovebox. For each substrate, 40 μL of the solution was spun at the 5000 rpm spin speed with 2500 rpm acceleration for 30 s. The samples were first dried at 150 °C then annealed at 300 °C for 1 h. After cooling to room temperature, the films were left in dry air in the dark overnight before the following steps. The expanded perovskite ((dmpz)Pb_2I_6 or (H_2apy)Pb_2I_6) layers were deposited as described in the previous section.

A thin layer of PCBM (40 nm) was spin-coated with modifications to a previous report.[63] Powder of PCBM (4.4 mg) was stirred in chlorobenzene (200 μL) until complete dissolution was observed. Immediately after filtration, 40 μL of the solution was spin-coated onto the sample at 1800 rpm with an acceleration rate of 1000 rpm/s for 35 s. When depositing, the solution was dropped evenly across the substrate, allowing for optimal wetting prior to spinning. The film was then annealed at 100 °C for 20 min.

The layer of BCP was thermally evaporated (Angstrom Amod) at 0.3 Å/s until it reached the final thickness of 7.5 nm. The Ag electrode layer was thermally evaporated through a patterned shadow mask revealing two active areas per sample, each 0.21 cm^2. The layer of Ag (Kurt J. Lesker) was first deposited at 0.3 Å/s until a thickness of 10 nm, then 1.0 Å/s until a thickness of 30 nm, then 3.0 Å/s until reaching the final thickness of 150 nm.

For the control devices, testing the quality of the (MA)PbI_3 thin films, solar cells of similar structure were fabricated. However, due to the energy levels of (MA)PbI_3, C_{60} was chosen as the better electron-transport layer instead of PCBM. All other fabrication steps were the same, except that the PCBM layer was replaced by C_{60}, which was thermally evaporated first at 0.3 Å/s until a thickness of 10 nm, then 0.6 Å/s until reaching the final thickness of 40 nm.

4.8. Single-Crystal X-ray Diffraction (SCXRD)

Crystals were transferred from the mother liquor onto clean glass substrate and dispersed with Paratone-N oil. A crystal of appropriate size was picked and mounted onto a Bruker D8 Venture diffractometer equipped with a Photon 100 CMOS detector. The radiation source was Mo Kα radiation (λ = 0.71073 Å). The measurements were taken at 100 K. The crystals did not show significant decay during data collection. Frames were collected using ω and φ scans and unit-cell parameters were refined against all data. Frames were integrated and corrected using SAINT V8.41 for Lorentz and polarization effects.[64] The absorption corrections were performed using SADABS-2016/2. Space-group assignments were based upon systematic absences, *E*-statistics, agreement factors for equivalent reflections, and successful refinement

Downloaded from pubs.acs.org/acscii/article-pdf/doi/10.1021/acscentsci.6c01379/6918706/acscentsci.6c01379.pdf by STANFORD UNIV user on 13 November 2026

https://doi.org/10.1021/acscentsci.6c01379
ACS Cent. Sci. XXXX, XXX, XXX−XXX

of the structures. The structures were solved using the intrinsic phasing method implemented in SHELXT 2018/2.[65] The solutions were refined against all data using the SHELXL 2019/3 software package[66] and OLEX2.[67] Weighted R factors, R_w, and all goodness-of-fit indicators are based on F^2. A small number of reflections with large errors were omitted from the refinements. The crystal was refined as a 2-component inversion twin. The occupancies of disordered iodide atoms were first permitted to refine freely and isotropically, and the occupancy of each part was fixed at a value similar to the freely refined occupancies (50%) that allowed all disordered atoms to reach a stable refinement. Several ISOR commands were used to stabilize the anisotropic refinement of disordered atoms and ensure that all disordered atoms could be refined to the same occupancy. Hydrogen atoms were inserted at idealized positions and refined using a riding model with an isotropic displacement parameter 1.2 times that of the attached carbon or nitrogen atoms.

4.9. Powder X-ray Diffraction (PXRD)

Diffraction patterns were collected under ambient conditions on a Bruker D8 Advance diffractometer using a Cu anode source (Cu Kα radiation, $K_{\alpha1}$ = 1.54060 Å, $K_{\alpha2}$ = 1.54443 Å, $K_{\alpha2}/K_{\alpha1}$ = 0.5), fixed divergence slits with a nickel filter, and a LYNXEYE 1D detector. The diffractometer operated under Bragg−Brentano geometry. The powders were dispersed in toluene and transferred to a clean glass slide. Pawley refinements (Figure S7) were performed in the GSAS-II software.[68] Simulated powder patterns were calculated directly from the crystallographic information files (CIFs) using the Mercury Software.

4.10. UV−Vis Spectroscopy

For thin films, absorption measurements were taken using the Cary 6000i UV−vis−NIR spectrophotometer or the Shimadzu UV-2600 spectrometer in transmission mode under ambient atmosphere. The absorption coefficient was extracted from absorbance using the following equation:

$$\alpha = 2.303\frac{A}{t}$$

where α is the absorption coefficient, A is the absorbance, and t is the film thickness.

For the temperature-dependent measurements, samples were cooled using liquid nitrogen with a Janis ST-100 cryostat. A Lakeshore Autotune temperature controller equipped with a PID loop was used to set the temperature.

4.11. Photothermal Deflection Spectroscopy (PDS)

PDS measurements used a previously reported setup.[69] Briefly, a pumped, monochromatic light source was aligned at normal incidence to a thin-film sample surface, and a probing laser beam was aligned transverse to the pumping beam (i.e., parallel to the sample surface). The pump source was the monochromated output from a halogen lamp modulated at 1 Hz. The probing laser beam was a helium−neon (HeNe) laser (632.8 nm, 1.5 mW output, less than 0.2% intensity fluctuation). The probing laser beam deflection was measured with a position sensitive silicon detector (Hamamatsu Photonics). The deflection signal was measured with a Stanford Research Systems SR830 lock-in amplifier. Samples were suspended in a filtered and degassed perfluorohexane solution (C_6F_{14}, 3 M Fluorinert FC-72) in a custom gastight chamber. All sample loading took place in a nitrogen glovebox.

PDS and UV−vis data were combined by comparing the slope of the two spectra. For a region where the two spectra showed the same slope, the PDS data were manually scaled appropriately to combine with the UV−vis data. In the final reported PDS spectra, the higher-energy data (>1.86 eV for (dmpz)Pb_2I_6 and >2.22 eV for (H_2apy)Pb_2I_6) are from UV−vis measurements, whereas the lower-energy data (<1.86 eV for (dmpz)Pb_2I_6 and <2.22 eV for (H_2apy)Pb_2I_6) are from PDS measurements.

4.12. Ultraviolet Photoelectron Spectroscopy (UPS) and Inverse Photoemission Spectroscopy (IPES)

UPS measurements were carried out using an excitation source of 10.2 eV vacuum-UV photons generated from an Excitech Hydrogen Lyman-α lamp emission with a pass energy of 5.85 eV. A PHI 5600 UHV system was used with a base pressure of $<4 \times 10^{-10}$ mbar to maintain ultrahigh vacuum. During measurements, all samples were biased at −5 V and are presented with the VBM at 0 eV.

IPES measurements were carried out in Bremsstrahlung isochromat mode with electron kinetic energies below 5 eV. An emission current of 2 μA was set to reduce sample damage. A Kimball Physics ELG-2 electron gun equipped with a low-temperature (1150 K) BaO cathode was used to generate the low-energy electron beam. Emitted photons were collected with a photon detector, which consisted of an optical bandpass filter (254 nm, Semrock) and a photomultiplier tube (R585, Hamamatsu Photonics). All samples were biased at −20 V. The ultrahigh vacuum chamber was kept dark to prevent external light exposure throughout the experiments.

For the UPS spectrum, the Secondary Electron Cut-off (SECO) energy and valence-band maximum (VBM) onset were extracted using linear extrapolation (Figure S1B,C). The onset of the IPES spectrum corresponds to the IB, which is dominated by organic molecular orbitals and not considered as three-dimensional. Therefore, the IB energy is extracted by fitting the onset with linear extrapolation. The entire IPES spectrum was fitted with the minimum number of Gaussian functions possible, with a constrained width (σ = 424 meV, where σ is the standard deviation of the Gaussian). The energy of the conduction-band minimum (CBM) was extracted by subtracting 2.9σ from the Gaussian peak position and found to be 2.33 eV.[70]

4.13. Attenuated Total Reflectance Fourier Transform Infrared (ATR-FTIR) Spectroscopy

IR spectra were collected on a ThermoScientific Nicolet iS50 FT-IR. For thin-film samples, the powder was scraped from the substrate using a clean razor blade. The measurements were conducted under ambient atmosphere.

4.14. Electronic Structure Calculations

Density functional theory (DFT) calculations were performed using the QUANTUM ESPRESSO simulation package.[41,42] Norm-conserving fully relativistic pseudopotentials were used for both (dmpz)Pb_2I_6 and (H_2apy)Pb_2I_6, obtained from PseudoDojo.[71] To determine the ground-state energy of the system we used a plane wave basis set with an energy cutoff of 70 and 80 Ry for (dmpz)Pb_2I_6 and (H_2apy)Pb_2I_6, respectively. The Brillouin zone was sampled using a 1 × 4 × 6 $\boldsymbol{k}$-grid consisting of 12 irreducible $\boldsymbol{k}$-points for (dmpz)Pb_2I_6 and a 1 × 4 × 2 $\boldsymbol{k}$-grid consisting of 6 irreducible $\boldsymbol{k}$-points for (H_2apy)Pb_2I_6. Spin−orbit-coupling (SOC) was considered self-consistently in all calculations excluding structural optimizations where the energy cutoff and the $\boldsymbol{k}$-grid used was the same as for the calculation of the ground state energy. The exchange-correlation functional used for all DFT calculations was the PBE functional.[72] For the density functional perturbation theory (DFPT) calculation of (dmpz)Pb_2I_6, a 1 × 4 × 6 $\boldsymbol{k}$-grid was used consisting of 12 irreducible $\boldsymbol{k}$-points. The vibrational density of states (VDOS) of Figure S14 was calculated only for the Γ point in the Brillouin zone. Eigenvalues and wave functions obtained from the DFT−PBE+SOC calculations were used to construct the one-particle Green's function G_0 and the screened Coulomb interaction W_0. G_0 and W_0 were subsequently used to obtain a converged quasiparticle band gap using the BerkeleyGW simulation package.[43,44]

For the G_0W_0 calculations of (dmpz)Pb_2I_6, we used 700 bands for the construction of the polarizability matrix and the self-energy matrix, an 8 Ry energy cutoff for the dielectric matrix and the Godby−Needs generalized plasmon pole (GPP) model,[73] while for (H_2apy)Pb_2I_6 the values were 700 bands and 4 Ry, respectively. With these settings, the macroscopic dielectric function ε_∞ is converged within 0.05 and the QP band gap within less than 0.1 eV (Figures S2 and S4). The optical properties of (dmpz)Pb_2I_6 were obtained by solving the Bethe−Salpeter equation (BSE) using the Tamm−Dancoff approximation (TDA).[74] The electron−hole interaction kernel $\boldsymbol{K}_{eh}$ was expanded

Downloaded from pubs.acs.org/acscii/article-pdf/doi/10.1021/acscentsci.6c01379/6918706/acscentsci.6c01379.pdf by STANFORD UNIV user on 13 November 2026

https://doi.org/10.1021/acscentsci.6c01379
ACS Cent. Sci. XXXX, XXX, XXX−XXX

using 20 valence bands and 25 conduction bands while interpolating a 1 × 4 × 6 ***k***-grid to a 4 × 10 × 12 ***k***-grid. The solution of the BSE was computed for 12 valence and 12 conduction bands. With these settings, the exciton binding energy was converged to within <5 meV with respect to the number of bands and ***k***-points included in the solution of the BSE (Figure S3).

4.15. Molecular Dynamics (MD) Calculations

MD simulations were performed with the Vienna-Ab-Initio Simulation Package (VASP)[75−77] using a plane wave basis and projector augmented wave (PAW) pseudopotentials.[78] We used the PBE functional[72] with Tkatchenko−Scheffler dispersion corrections.[79,80] To accelerate the MD simulations, machine-learned force fields were trained on-the-fly[81] using the Gaussian approximation potential[82] with two- and three-body atomic descriptors based on the smooth overlap of atomic orbitals (SOAP) method.[83] The electronic minimization was performed using a 400 eV plane wave cutoff energy and a 1 × 2 × 4 ***k***-point grid. The MD simulation was performed under isothermal and isobaric conditions (*NpT*) at 300 K for 10 ps on the 52-atom unit-cell of the (dmpz)Pb_2I_6 structure. With these settings we achieve an average error of 0.662 meV/atom for the energies and 52.32 meV/Å for the forces, falling within the typical error ranges reported for modern machine-learning interatomic potentials, which are on the order of 1−10 meV/atom error for the energies and 20−40 meV/Å for the forces, respectively.[84] Additionally, we find that 10 ps of simulation time is enough for the system to equilibrate as seen by the temperature reaching a plateau around 3 ps in Figure S5A.

From the last ps of the equilibrated MD trajectory, we extracted 100 MD snapshots with 10 fs spacing and performed G_0W_0+BSE calculations with the same convergence criteria as described in the previous section. It is important to note that while the structures were generated using MD performed in VASP, the calculations for the study of the electronic structure and the optical properties were performed using QUANTUM ESPRESSO and BerkeleyGW. We assessed statistical convergence of the ensemble-averaged band gap using bootstrap resampling (10,000 replicates per sample size). We find that for number of snapshots larger than 80, the bootstrap standard error of the mean falls below 0.02 eV, corresponding to <2% of the converged ensemble-averaged band gap (1.46 eV), as shown in Figure S5B.

4.16. Raman Spectroscopy

The continuous-wave Raman measurements were conducted using a Renishaw inVia Raman confocal microscope with a 633 nm excitation laser. Severe Rayleigh scattering prevents measurement of mode frequencies below ∼100 cm^{-1}. To access low-frequency modes down to 25 cm^{-1}, Raman spectra were collected with a HORIBA T64000 spectrometer with a triple-grating configuration, using a 785 nm excitation laser.

4.17. Transient Absorption (TA) Spectroscopy

A broad ultraviolet−visible spectrum ranging from 400 to 700 nm was generated by pumping a CaF_2 crystal with the output of an 800 nm Ti:sapphire laser (Spectra Physics Solstice Ace, 7 W, 1 kHz repetition rate, 100 fs) and collimating after it. Various narrowband pump wavelengths were generated using the same laser output. First, 400 nm (3.1 eV) was generated through second harmonic generation of the 800 nm output using a β-barium borate crystal. This 400 nm pulse also serves as the pump for the noncollinear parametric amplification (NOPA) to generate the 500 nm (2.48 eV) and 610 nm (2.03 eV) pumps. The 400 nm pump is mixed with a chirped white-light supercontinuum seed pulse, generated by focusing the 800 nm fundamental into a sapphire crystal and passing it through a 20 mm of quartz, into a BBO crystal to create the amplified 500 or 610 nm signal wavelengths depending on the temporal overlap of the 400 nm pump with respect to the white light. To minimize pump scatter, an ultrabroadband wire grid polarizer (Thorlabs) was placed in the detection path. For the nanosecond TA measurements, the pump−probe delay was electronically controlled rather than mechanically controlled. The 400 nm pump was generated as described above, and the broadband white-light probe was produced using a Disco supercontinuum laser (Leukos Laser, STM-2-UV).

4.18. Impulsive Vibrational Spectroscopy (IVS)

A chirped white light continuum (WLC) spectrum spanning 530−950 nm, serving as the probe beam, was generated by focusing part of the 1030 nm fundamental output from a Yb:KGW amplifier laser (Light Conversion Pharos, 14.5 W, 38 kHz repetition rate, 200 fs) onto a 3 mm YAG crystal, followed by a collimation. The pump beam was produced through noncollinear optical parametric amplification (NOPA) of a 1030-WLC (TAG for SH, Sapphire for TH) using either the second (515 nm) or third harmonic (343 nm), which were generated by an automatic harmonic generator (Light Conversion HIRO). These pulses achieved durations of 11 fs with spectra spanning 500−650 nm when amplified by the third harmonic, and 13 fs with spectra spanning 650−900 nm when amplified by the second harmonic. Compression of the pump pulses was achieved using a pair of chirped mirrors in combination with wedge prisms (Layertec). The spatiotemporal profiles of these pulses were characterized via second-harmonic generation frequency-resolved optical gating (SHG-FROG). Differential transmission spectra were obtained by modulating the pump beam at 9 kHz with a chopper wheel. A computer-controlled piezoelectric translation stage (Physik Instrumente) with a 4 fs step size was used to set the pump−probe delay. To minimize pump scatter, an ultrabroadband wire grid polarizer (Thorlabs) was placed in the detection path. The transmitted probe was measured using a grating spectrometer equipped with a Silicon camera (Entwicklungsbüro Stresing) operating at 38 kHz and a 550 nm blazed grating. A frequency scaling factor was applied to the FFT spectra to take into account the effect of time resolution on the intensity.[85]

4.19. Top-View Scanning Electron Microscopy (SEM)

Perovskite and expanded perovskite-analog thin films deposited on planar ITO substrates were used for top-view SEM imaging. Samples were mounted on appropriate-sized SEM pins (Ted Pella) using conductive carbon glue or silver paint (Ted Pella). Measurements were performed on a Thermo Fisher Scientific Apreo S LoVac or a FEI Magellan 400 XHR scanning electron microscope with a field-emission gun (FEG) under vacuum, using imaging conditions of 5 kV voltage and 25 pA current.

4.20. Cross-Sectional SEM

Solar-cell devices were carefully cut into smaller pieces using a diamond pen, exposing a clean-cut cross section in the active area. The samples were mounted on a double 90° SEM mount (Ted Pella) with the material side facing the metal mount using conductive silver paint (Ted Pella). Measurements were performed on an FEI Magellan 400 XHR scanning electron microscope with a FEG source under vacuum, using imaging conditions of 2 kV voltage and 25 pA current. Each scan has an acquisition time of 200 ns, the scan line is interlaced every 5 rows, and integrated with 100 frames.

4.21. Current−Voltage (*J*−*V*) Measurement

J−*V* measurements of the unencapsulated perovskite cells were performed under ambient conditions at 1-sun, AM 1.5G illumination. The illumination condition was achieved using a solar simulator (Photo Emission Tech Class AAA) with a xenon arc lamp, calibrated with a Si reference cell (Photo Emission Tech Model 60909). The *J*−*V* curves were measured using a Keithley 2420 sourcemeter, with a scanning speed of 500 mV/s for higher-conductivity materials ($(H_2apy)Pb_2I_6$ and $(MA)PbI_3$ and 200 mV/s for (dmpz)Pb_2I_6. The scan direction was from forward to reverse bias.

4.22. External Quantum Efficiency (EQE) and Two-Photon Photocurrent (TPPC) Measurement

For the EQE measurements, an Xe lamp (ThorLabs HPLS-30-03) and monochromator (Newport Cornerstone 130 monochromator) were used as the light source for the primary light, scanning from 900 to 400 nm with 5 nm intervals. A 650 nm long pass filter was used to eliminate second-order diffraction effects at longer wavelengths. The filter was inserted on the light path when scans were automatically paused at 675 nm. The light from the monochromator passes through an optical chopper modulated at 222 Hz (Stanford Research Systems Model SR540 chopper controller). The photocurrent was collected using a

https://doi.org/10.1021/acscentsci.6c01379
ACS Cent. Sci. XXXX, XXX, XXX−XXX

Downloaded from pubs.acs.org/acscii/article-pdf/doi/10.1021/acscentsci.6c01379/6918706/acscentsci.6c01379.pdf by STANFORD UNIV user on 13 November 2026

lock-in amplifier (Stanford Research systems SR860 500 kHz DSP lock-in amplifier). For each wavelength, 10 data points were taken with a 0.1 s interval, and the averaged value was then recorded for the wavelength. There was a 0.2 s sleep time for the current to stabilize between each wavelength. The spot size of the incident beam was measured using Thorlabs CS165CU-Zelux 1.6 MP Color CMOS Camera.

For TPPC measurements, an IR bias of 980 nm (ThorLabs S1FC980 Fabry−Perot benchtop laser source) was used at 0.157 W/cm^2. The samples were measured with the IR bias off once, with the IR bias on twice, and with the IR bias off once, consecutively. The IR on and off scans were averaged to reduce the effects of additional factors such as laser heating of the samples. The ΔEQE is computed as the difference between averaged EQE with IR on and IR off scans.

4.23. Power Dependence

Measurements were performed using a laser with wavelengths of 637 nm (1.94 eV, ThorLabs S4FC637), 980 nm (1.26 eV, ThorLabs S1FC980), and 1208 nm (1.03 eV, Changchun New Industries Optoelectronics Co., Ltd.). The IR light was chopped at 220 Hz (Stanford Research Systems Model SR540 chopper controller). A neutral density (ND) filter wheel was placed in front of the laser to adjust the incident intensity on the sample. The spot size of the incident beam was measured using a Thorlabs CS165CU-Zelux 1.6 MP Color CMOS Camera. The incident laser power was recorded using a power meter before each measurement (ThorLabs PM 100D power meter console; for 637 and 980 nm light, a Newport 818-SL detector without an external attenuator was used; for 1208 nm light, a Newport 818-IR detector with an external attenuator was used). At each laser intensity, 20 measurements were taken with a 0.1 s separation. The average values and standard deviations were extracted and plotted.

4.24. Profilometry

The film thickness was measured with a Bruker Dektak XT-A profilometer using a stylus force of 3. Each film was measured five times, and the average thickness was recorded.

4.25. Humidity Stability Tests

The expanded perovskite-analog thin films were loaded on PXRD pucks and placed in a closed glass chamber wrapped with electrical tape to avoid light exposure. A relative humidity (RH) of 76% was maintained in the chamber using N_2 that was bubbled through DI water and then through a saturated sodium chloride (NaCl) in DI water solution.

■ ASSOCIATED CONTENT

Data Availability Statement

The data that support the findings of this study are openly available in the Stanford Digital Repository at 10.25740/cj618ft5257. The crystallographic data for $(H_2apy)Pb_2I_6$ reported in this article have been deposited at the Cambridge Crystallographic Data Centre under deposition number CCDC 2571283. These data can be obtained free of charge via https://www.ccdc.cam.ac.uk/structures.

Supporting Information

The Supporting Information is available free of charge at https://pubs.acs.org/doi/10.1021/acscentsci.6c01379.

Crystallographic data for $(H_2apy)Pb_2I_6$ (CIF)

Additional crystallographic data, experimental and calculation details, spectra, and further discussion are provided in Tables S1 and S2, Figures S1−S45, and Supplementary Notes 1−6 (PDF)

Supplementary Video 1 (GIF)

Supplementary Video 2 (GIF)

Supplementary Video 3 (GIF)

■ AUTHOR INFORMATION

Corresponding Authors

Hemamala I. Karunadasa − *Department of Chemistry, Stanford University, Stanford, California 94305, United States; Stanford Institute for Materials and Energy Sciences, SLAC National Laboratory, Menlo Park, California 94025, United States;* orcid.org/0000-0003-4949-8068; Email: hemamala@stanford.edu

Linn Leppert − *School of Metallurgy and Materials, University of Birmingham, Edgbaston, Birmingham B15 2TT, United Kingdom; MESA+ Institute for Nanotechnology, University of Twente, 7522 NB Enschede, The Netherlands;* orcid.org/0000-0002-4361-4382; Email: l.leppert@bham.ac.uk

Authors

Zhiqiao Jiang − *Department of Chemistry, Stanford University, Stanford, California 94305, United States; Department of Materials Science and Engineering, Stanford University, Stanford, California 94305, United States*

Kostas Fykouras − *MESA+ Institute for Nanotechnology, University of Twente, 7522 NB Enschede, The Netherlands*

Yorrick Boeije − *Department of Chemical Engineering and Biotechnology, University of Cambridge, Cambridge CB3 0AS, United Kingdom; Department of Physics, Cavendish Laboratory, University of Cambridge, Cambridge CB3 0HE, United Kingdom*

Kyle Frohna − *Department of Materials Science and Engineering and Department of Electrical Engineering, Stanford University, Stanford, California 94305, United States*

Austin C. Flick − *Department of Materials Science and Engineering, Stanford University, Stanford, California 94305, United States*

Garrett LeCroy − *Department of Materials Science and Engineering, Stanford University, Stanford, California 94305, United States*

Syed Joy − *Department of Chemistry, University of Kentucky, Lexington, Kentucky 40506, United States*

Zhengkang Qu − *Department of Physics, Cavendish Laboratory, University of Cambridge, Cambridge CB3 0HE, United Kingdom*

Abigail Carbone − *Department of Materials Science and Engineering, Stanford University, Stanford, California 94305, United States*

Julian A. Vigil − *Department of Chemistry, Stanford University, Stanford, California 94305, United States;* orcid.org/0000-0002-0205-2379

Akshay Rao − *Department of Physics, Cavendish Laboratory, University of Cambridge, Cambridge CB3 0HE, United Kingdom;* orcid.org/0000-0003-4261-0766

Alberto Salleo − *Department of Materials Science and Engineering, Stanford University, Stanford, California 94305, United States*

Reinhold H. Dauskardt − *Department of Materials Science and Engineering, Stanford University, Stanford, California 94305, United States*

Samuel D. Stranks − *Department of Chemical Engineering and Biotechnology, University of Cambridge, Cambridge CB3 0AS, United Kingdom; Department of Physics, Cavendish Laboratory, University of Cambridge, Cambridge CB3 0HE, United Kingdom;* orcid.org/0000-0002-8303-7292

Downloaded from pubs.acs.org/acscii/article-pdf/doi/10.1021/acscentsci.6c01379/6918706/acscentsci.6c01379.pdf by STANFORD UNIV user on 13 November 2026

Kenneth R. Graham − *Department of Chemistry, University of Kentucky, Lexington, Kentucky 40506, United States;* orcid.org/0000-0002-6387-3998

Daniel N. Congreve − *Department of Chemistry, Stanford University, Stanford, California 94305, United States; Department of Electrical Engineering, Stanford University, Stanford, California 94305, United States;* orcid.org/0000-0002-2914-3561

Complete contact information is available at: https://pubs.acs.org/10.1021/acscentsci.6c01379

Author Contributions

†Co-second author.

Notes

The authors declare no competing financial interest.

■ ACKNOWLEDGMENTS

This work was supported by the Precourt Institute for Energy at Stanford University, with synthetic work supported by the Department of Energy, Office of Basic Energy Sciences, Division of Materials Sciences and Engineering, under Contract DE-AC02-76SF00515. Ko.F. and L.L. acknowledge funding by the Dutch Research Council (NWO) under Grant OCENW.M20.337. Y.B. acknowledges the Winton Programme for Physics of Sustainability for funding. S.D.S. acknowledges the Royal Society and Tata Group (Grants UF150033 and URF\R \221026). Ky.F. acknowledges funding from the Stanford Energy Postdoctoral Fellowship and the Precourt Institute for Energy. S.J. and K.R.G. acknowledge support from the National Science Foundation (NSF) under DMR-2102257. SCXRD, profilometry experiments, UV−vis absorption measurements, and SEM measurements were performed at nano@stanford RRID:SCR_026695. We thank Kai Hui Lui for preliminary investigation and Prof. Daiki Umeyama (National Institute for Materials, Japan), Prof. Roc Matheu (Universitat de Barcelona, Spain), and Dr. Sebastian Fernández for helpful discussions.

■ REFERENCES

(1) Shockley, W.; Queisser, H. J. Detailed Balance Limit of Efficiency of *p-n* Junction Solar Cells. *J. Appl. Phys.* **1961**, *32* (3), 510−519.

(2) Hu, Z.; Lin, Z.; Su, J.; Zhang, J.; Chang, J.; Hao, Y. A Review on Energy Band-Gap Engineering for Perovskite Photovoltaics. *Sol. RRL* **2019**, *3* (12), 1900304.

(3) Luque, A.; Martí, A. Increasing the Efficiency of Ideal Solar Cells by Photon Induced Transitions at Intermediate Levels. *Phys. Rev. Lett.* **1997**, *78* (26), 5014−5017.

(4) Luque, A.; Martí, A.; Stanley, C. Understanding Intermediate-Band Solar Cells. *Nat. Photonics* **2012**, *6* (3), 146−152.

(5) Ramiro, I.; Marti, A.; Antolin, E.; Luque, A. Review of Experimental Results Related to the Operation of Intermediate Band Solar Cells. *IEEE J. Photovoltaics* **2014**, *4* (2), 736−748.

(6) Okada, Y.; Ekins-Daukes, N. J.; Kita, T.; Tamaki, R.; Yoshida, M.; Pusch, A.; Hess, O.; Phillips, C. C.; Farrell, D. J.; Yoshida, K.; Ahsan, N.; Shoji, Y.; Sogabe, T.; Guillemoles, J. F. Intermediate Band Solar Cells: Recent Progress and Future Directions. *Appl. Phys. Rev.* **2015**, *2*, 021302.

(7) Ramiro, I.; Martí, A. Intermediate Band Solar Cells: Present and Future. *Prog. Photovoltaics Res. Appl.* **2021**, *29* (7), 705−713.

(8) Brown, A. S.; Green, M. A. Impurity Photovoltaic Effect: Fundamental Energy Conversion Efficiency Limits. *J. Appl. Phys.* **2002**, *92* (3), 1329−1336.

(9) Almansouri, I.; Ho-Baillie, A.; Bremner, S. P.; Green, M. A. Supercharging Silicon Solar Cell Performance by Means of Multi-junction Concept. *IEEE J. Photovoltaics* **2015**, *5*, 968−976.

(10) Linares, P. G.; Martí, A.; Antolín, E.; Ramiro, I.; López, E.; Hernández, E.; Fuertes Marrón, D.; Artacho, I.; Tobías, I.; Gérard, P.; Chaix, C.; Campion, R. P.; Foxon, C. T.; Stanley, C. R.; Molina, S. I.; Luque, A. Extreme Voltage Recovery in GaAs:Ti Intermediate Band Solar Cells. *Sol. Energy Mater. Sol. Cells* **2013**, *108*, 175−179.

(11) Sheu, J.-K.; Huang, F.-W.; Liu, Y.-H.; Chen, P. C.; Yeh, Y.-H.; Lee, M.-L.; Lai, W.-C. Photoresponses of Manganese-Doped Gallium Nitride Grown by Metalorganic Vapor-Phase Epitaxy. *Appl. Phys. Lett.* **2013**, *102* (7), 071107.

(12) Tanaka, T.; Yu, K. M.; Levander, A. X.; Dubon, O. D.; Reichertz, L. A.; Lopez, N.; Nishio, M.; Walukiewicz, W. Demonstration of $ZnTe_{1-x}O_x$ Intermediate Band Solar Cell. *Jpn. J. Appl. Phys.* **2011**, *50* (8R), 082304.

(13) Wang, W.; Lin, A. S.; Phillips, J. D. Intermediate-Band Photovoltaic Solar Cell Based on ZnTe:O. *Appl. Phys. Lett.* **2009**, *95* (1), 011103.

(14) Martí, A.; Antolín, E.; Stanley, C. R.; Farmer, C. D.; López, N.; Díaz, P.; Cánovas, E.; Linares, P. G.; Luque, A. Production of Photocurrent Due to Intermediate-to-Conduction-Band Transitions: A Demonstration of a Key Operating Principle of the Intermediate-Band Solar Cell. *Phys. Rev. Lett.* **2006**, *97* (24), 247701.

(15) Luque, A.; Martí, A.; Stanley, C.; López, N.; Cuadra, L.; Zhou, D.; Pearson, J. L.; McKee, A. General Equivalent Circuit for Intermediate Band Devices: Potentials, Currents and Electroluminescence. *J. Appl. Phys.* **2004**, *96* (1), 903−909.

(16) Shoji, Y.; Akimoto, K.; Okada, Y. Self-Organized InGaAs/GaAs Quantum Dot Arrays for Use in High-Efficiency Intermediate-Band Solar Cells. *J. Phys. D: Appl. Phys.* **2013**, *46* (2), 024002.

(17) Tamaki, R.; Shoji, Y.; Okada, Y.; Miyano, K. Spectrally Resolved Intraband Transitions on Two-Step Photon Absorption in InGaAs/GaAs Quantum Dot Solar Cell. *IEEE J. Photovoltaics* **2015**, *5* (1), 229−233.

(18) Kada, T.; Asahi, S.; Kaizu, T.; Harada, Y.; Kita, T.; Tamaki, R.; Okada, Y.; Miyano, K. Two-Step Photon Absorption in InAs/GaAs Quantum-Dot Superlattice Solar Cells. *Phys. Rev. B* **2015**, *91* (20), 201303.

(19) Hosokawa, H.; Tamaki, R.; Sawada, T.; Okonogi, A.; Sato, H.; Ogomi, Y.; Hayase, S.; Okada, Y.; Yano, T. Solution-Processed Intermediate-Band Solar Cells with Lead Sulfide Quantum Dots and Lead Halide Perovskites. *Nat. Commun.* **2019**, *10* (1), 43.

(20) Yang, C.; Qin, M.; Wang, Y.; Wan, D.; Huang, F.; Lin, J. Observation of an Intermediate Band in Sn-Doped Chalcopyrites with Wide-Spectrum Solar Response. *Sci. Rep.* **2013**, *3* (1), 1286.

(21) Menda, U. D.; Ribeiro, G.; Deuermeier, J.; López, E.; Nunes, D.; Jana, S.; Artacho, I.; Martins, R.; Mora-Seró, I.; Mendes, M. J.; Ramiro, I. Thermal-Carrier-Escape Mitigation in a Quantum-Dot-In-Perovskite Intermediate Band Solar Cell via Bandgap Engineering. *ACS Photonics* **2023**, *10* (10), 3647−3655.

(22) Tanabe, K.; Guimard, D.; Bordel, D.; Arakawa, Y. High-Efficiency InAs/GaAs Quantum Dot Solar Cells by Metalorganic Chemical Vapor Deposition. *Appl. Phys. Lett.* **2012**, *100* (19), 193905.

(23) Beattie, N. S.; See, P.; Zoppi, G.; Ushasree, P. M.; Duchamp, M.; Farrer, I.; Ritchie, D. A.; Tomić, S. Quantum Engineering of InAs/GaAs Quantum Dot Based Intermediate Band Solar Cells. *ACS Photonics* **2017**, *4* (11), 2745−2750.

(24) Ekins-Daukes, N. J.; Schmidt, T. W. A Molecular Approach to the Intermediate Band Solar Cell: The Symmetric Case. *Appl. Phys. Lett.* **2008**, *93* (6), 063507.

(25) Singh-Rachford, T. N.; Castellano, F. N. Photon Upconversion Based on Sensitized Triplet-Triplet Annihilation. *Coord. Chem. Rev.* **2010**, *254* (21−22), 2560−2573.

(26) Simpson, C.; Clarke, T. M.; MacQueen, R. W.; Cheng, Y. Y.; Trevitt, A. J.; Mozer, A. J.; Wagner, P.; Schmidt, T. W.; Nattestad, A. An Intermediate Band Dye-Sensitised Solar Cell Using Triplet-Triplet Annihilation. *Phys. Chem. Chem. Phys.* **2015**, *17* (38), 24826−24830.

(27) Lin, Y. H. L.; Koch, M.; Brigeman, A. N.; Freeman, D. M. E.; Zhao, L.; Bronstein, H.; Giebink, N. C.; Scholes, G. D.; Rand, B. P. Enhanced Sub-Bandgap Efficiency of a Solid-State Organic Inter-

Downloaded from pubs.acs.org/acscii/article-pdf/doi/10.1021/acscentsci.6c01379/6918706/acscentsci.6c01379.pdf by STANFORD UNIV user on 13 November 2026

mediate Band Solar Cell Using Triplet-Triplet Annihilation. *Energy Environ. Sci.* **2017**, *10* (6), 1465−1475.
(28) Birks, J. B. The Quintet State of the Pyrene Excimer. *Phys. Lett. A* **1967**, *24* (9), 479−480.
(29) Naimovičius, L.; Bharmoria, P.; Moth-Poulsen, K. Triplet-Triplet Annihilation Mediated Photon Upconversion Solar Energy Systems. *Mater. Chem. Front.* **2023**, *7* (12), 2297−2315.
(30) Umeyama, D.; Leppert, L.; Connor, B. A.; Manumpil, M. A.; Neaton, J. B.; Karunadasa, H. I. Expanded Analogs of Three-Dimensional Lead-Halide Hybrid Perovskites. *Angew. Chemie Int. Ed.* **2020**, *59* (43), 19087−19094.
(31) Shores, M. P.; Beauvais, L. G.; Long, J. R. Cluster-Expanded Prussian Blue Analogues. *J. Am. Chem. Soc.* **1999**, *121* (4), 775−779.
(32) Zhang, H.-Y.; Song, X.-J.; Cheng, H.; Zeng, Y.-L.; Zhang, Y.; Li, P.-F.; Liao, W.-Q.; Xiong, R.-G. A Three-Dimensional Lead Halide Perovskite-Related Ferroelectric. *J. Am. Chem. Soc.* **2020**, *142* (10), 4604−4608.
(33) Li, X.; He, Y.; Kepenekian, M.; Guo, P.; Ke, W.; Even, J.; Katan, C.; Stoumpos, C. C.; Schaller, R. D.; Kanatzidis, M. G. Three-Dimensional Lead Iodide Perovskitoid Hybrids with High X-Ray Photoresponse. *J. Am. Chem. Soc.* **2020**, *142* (14), 6625−6637.
(34) Mitzi, D. B.; Chondroudis, K.; Kagan, C. R. Design, Structure, and Optical Properties of Organic-Inorganic Perovskites Containing an Oligothiophene Chromophore. *Inorg. Chem.* **1999**, *38* (26), 6246−6256.
(35) Liu, C.; Huhn, W.; Du, K.-Z.; Vazquez-Mayagoitia, A.; Dirkes, D.; You, W.; Kanai, Y.; Mitzi, D. B.; Blum, V. Tunable Semiconductors: Control over Carrier States and Excitations in Layered Hybrid Organic-Inorganic Perovskites. *Phys. Rev. Lett.* **2018**, *121* (14), 146401.
(36) Reynolds, R. P.; Persaud, J. H.; Volonakis, G.; Torma, A. J.; Meza, P. E.; Kelly, Z. E.; Stoumpos, C. C.; Dravid, V. P.; Katan, C.; Mohite, A. D.; Kanatzidis, M. G. Design Principles for Narrow-Gap Hybrid Semiconductors: Insights from Viologen-Tin and Viologen-Lead Iodides. *J. Am. Chem. Soc.* **2025**, *147* (28), 24573−24593.
(37) Deschene, C. R.; Ke, F.; Fykouras, K.; Su, A. C.; Lin, Y.; Leppert, L.; Karunadasa, H. I.; Matheu, R. Pyridinium Cations Act as Charge Reservoirs in Expanded Halide Perovskite Analogs at High Pressure. *Angew. Chemie Int. Ed.* **2026**, *65* (43), No. e2495859.
(38) Matheu, R.; Ke, F.; Breidenbach, A.; Wolf, N. R.; Lee, Y.; Liu, Z.; Leppert, L.; Lin, Y.; Karunadasa, H. I. Charge Reservoirs in an Expanded Halide Perovskite Analog: Enhancing High-Pressure Conductivity through Redox-Active Molecules. *Angew. Chemie Int. Ed.* **2022**, *61* (25), No. e202202911.
(39) Wei, X.; Xia, J.; Cai, B.; Wang, N. Intermediate-Band Engineering in Halide Perovskites for Multi-Junction-Competitive Single-Junction Photovoltaics. *Mater. Today Chem.* **2026**, *53*, 103480.
(40) Golze, D.; Dvorak, M.; Rinke, P. The *GW* Compendium: A Practical Guide to Theoretical Photoemission Spectroscopy. *Front. Chem.* **2019**, *7*, 377.
(41) Giannozzi, P.; Baroni, S.; Bonini, N.; Calandra, M.; Car, R.; Cavazzoni, C.; Ceresoli, D.; Chiarotti, G. L.; Cococcioni, M.; Dabo, I.; Dal Corso, A.; de Gironcoli, S.; Fabris, S.; Fratesi, G.; Gebauer, R.; Gerstmann, U.; Gougoussis, C.; Kokalj, A.; Lazzeri, M.; Martin-Samos, L.; Marzari, N.; Mauri, F.; Mazzarello, R.; Paolini, S.; Pasquarello, A.; Paulatto, L.; Sbraccia, C.; Scandolo, S.; Sclauzero, G.; Seitsonen, A. P.; Smogunov, A.; Umari, P.; Wentzcovitch, R. M. QUANTUM ESPRESSO: A Modular and Open-Source Software Project for Quantum Simulations of Materials. *J. Phys.: Condens. Matter* **2009**, *21* (39), 395502.
(42) Giannozzi, P.; Andreussi, O.; Brumme, T.; Bunau, O.; Buongiorno Nardelli, M.; Calandra, M.; Car, R.; Cavazzoni, C.; Ceresoli, D.; Cococcioni, M.; Colonna, N.; Carnimeo, I.; Dal Corso, A.; de Gironcoli, S.; Delugas, P.; DiStasio, R. A.; Ferretti, A.; Floris, A.; Fratesi, G.; Fugallo, G.; Gebauer, R.; Gerstmann, U.; Giustino, F.; Gorni, T.; Jia, J.; Kawamura, M.; Ko, H.-Y.; Kokalj, A.; Küçükbenli, E.; Lazzeri, M.; Marsili, M.; Marzari, N.; Mauri, F.; Nguyen, N. L.; Nguyen, H.-V.; Otero-de-la-Roza, A.; Paulatto, L.; Poncé, S.; Rocca, D.; Sabatini, R.; Santra, B.; Schlipf, M.; Seitsonen, A. P.; Smogunov, A.; Timrov, I.; Thonhauser, T.; Umari, P.; Vast, N.; Wu, X.; Baroni, S. Advanced Capabilities for Materials Modelling with Quantum ESPRESSO. *J. Phys.: Condens. Matter* **2017**, *29* (46), 465901.
(43) Deslippe, J.; Samsonidze, G.; Strubbe, D. A.; Jain, M.; Cohen, M. L.; Louie, S. G. BerkeleyGW: A Massively Parallel Computer Package for the Calculation of the Quasiparticle and Optical Properties of Materials and Nanostructures. *Comput. Phys. Commun.* **2012**, *183* (6), 1269−1289.
(44) Barker, B. A.; Deslippe, J.; Lischner, J.; Jain, M.; Yazyev, O. V.; Strubbe, D. A.; Louie, S. G. Spinor GW/Bethe-Salpeter Calculations in BerkeleyGW: Implementation, Symmetries, Benchmarking, and Performance. *Phys. Rev. B* **2022**, *106* (11), 115127.
(45) Filip, M. R.; Giustino, F. *GW* Quasiparticle Band Gap of the Hybrid Organic-Inorganic Perovskite $CH_3NH_3PbI_3$: Effect of Spin-Orbit Interaction, Semicore Electrons, and Self-Consistency. *Phys. Rev. B* **2014**, *90* (24), 245145.
(46) Leppert, L.; Rangel, T.; Neaton, J. B. Towards Predictive Band Gaps for Halide Perovskites: Lessons from One-Shot and Eigenvalue Self-Consistent *GW*. *Phys. Rev. Mater.* **2019**, *3* (10), 103803.
(47) Boeije, Y.; Van Gompel, W. T. M.; Zhang, Y.; Ghosh, P.; Zelewski, S. J.; Maufort, A.; Roose, B.; Ooi, Z. Y.; Chowdhury, R.; Devroey, I.; Lenaers, S.; Tew, A.; Dai, L.; Dey, K.; Salway, H.; Friend, R. H.; Sirringhaus, H.; Lutsen, L.; Vanderzande, D.; Rao, A.; Stranks, S. D. Tailoring Interlayer Charge Transfer Dynamics in 2D Perovskites with Electroactive Spacer Molecules. *J. Am. Chem. Soc.* **2023**, *145* (39), 21330−21343.
(48) Tao, W.; He, G.; Feng, Q.; Wang, Y.; Li, T.; Li, Y.; Shi, E.; Nan, G.; Zhu, H. Direct Charge-Transfer Transition Drives Triplet Generation and Photon Upconversion in 2D Hybrid Perovskites. *J. Am. Chem. Soc.* **2025**, *147* (51), 47280−47288.
(49) Xing, G.; Mathews, N.; Sun, S.; Lim, S. S.; Lam, Y. M.; Grätzel, M.; Mhaisalkar, S.; Sum, T. C. Long-Range Balanced Electron- and Hole-Transport Lengths in Organic-Inorganic $CH_3NH_3PbI_3$. *Science* **2013**, *342* (6156), 344−347.
(50) Schiettecatte, P.; Hens, Z.; Geiregat, P. A Roadmap to Decipher Ultrafast Photophysics in Two-Dimensional Nanomaterials. *J. Chem. Phys.* **2023**, *158* (1), 014202.
(51) Ramesh, S.; Wang, Y.; Chabera, P.; Araujo, R.; Aboulsaad, M.; Edvinsson, T.; Gao, F.; Pullerits, T. Coherent Phonons, Localization, and Slow Polaron Formation in Lead-Free Gold Perovskite. *Adv. Opt. Mater.* **2025**, *13* (10), 2402882.
(52) Hilgers, F.; Kaim, W.; Schulz, A.; Záliš, S. Electronic Absorption Spectroscopy of Some Exceptionally Stable 1,4-Dialkyl-1,4-Dihydro-1,4-Diazinium Radical Cations: Assignment of Transitions, Vibrational Structure and Effects of π-π Dimerization. *J. Chem. Soc. Perkin Trans. 2* **1994**, *23* (1), 135−138.
(53) Zhang, X.; Wang, M.-S.; Sun, C.; Yang, C.; Li, P.-X.; Guo, G.-C. Stabilizing and Color Tuning Pyrazine Radicals by Coordination for Photochromism. *Chem. Commun.* **2016**, *52* (51), 7947−7949.
(54) Batignani, G.; Fumero, G.; Srimath Kandada, A. R.; Cerullo, G.; Gandini, M.; Ferrante, C.; Petrozza, A.; Scopigno, T. Probing Femtosecond Lattice Displacement upon Photo-Carrier Generation in Lead Halide Perovskite. *Nat. Commun.* **2018**, *9* (1), 1971.
(55) Thouin, F.; Valverde-Chávez, D. A.; Quarti, C.; Cortecchia, D.; Bargigia, I.; Beljonne, D.; Petrozza, A.; Silva, C.; Srimath Kandada, A. R. Phonon Coherences Reveal the Polaronic Character of Excitons in Two-Dimensional Lead Halide Perovskites. *Nat. Mater.* **2019**, *18* (4), 349−356.
(56) Park, M.; Neukirch, A. J.; Reyes-Lillo, S. E.; Lai, M.; Ellis, S. R.; Dietze, D.; Neaton, J. B.; Yang, P.; Tretiak, S.; Mathies, R. A. Excited-State Vibrational Dynamics toward the Polaron in Methylammonium Lead Iodide Perovskite. *Nat. Commun.* **2018**, *9* (1), 2525.
(57) Noh, J. H.; Im, S. H.; Heo, J. H.; Mandal, T. N.; Seok, S. Il. Chemical Management for Colorful, Efficient, and Stable Inorganic-Organic Hybrid Nanostructured Solar Cells. *Nano Lett.* **2013**, *13* (4), 1764−1769.
(58) Smith, I. C.; Hoke, E. T.; Solis-Ibarra, D.; McGehee, M. D.; Karunadasa, H. I. A Layered Hybrid Perovskite Solar-Cell Absorber with Enhanced Moisture Stability. *Angew. Chemie Int. Ed.* **2014**, *53* (42), 11232−11235.

Downloaded from pubs.acs.org/acscii/article-pdf/doi/10.1021/acscentsci.6c01379/6918706/acscentsci.6c01379.pdf by STANFORD UNIV user on 13 November 2026

https://doi.org/10.1021/acscentsci.6c01379
ACS Cent. Sci. XXXX, XXX, XXX−XXX

(59) van Gorkom, B. T.; van der Pol, T. P. A.; Datta, K.; Wienk, M. M.; Janssen, R. A. J. Revealing Defective Interfaces in Perovskite Solar Cells from Highly Sensitive Sub-Bandgap Photocurrent Spectroscopy Using Optical Cavities. *Nat. Commun.* **2022**, *13*, 349.
(60) van Gorkom, B. T.; Simons, A.; Remmerswaal, W. H. M.; Wienk, M. M.; Janssen, R. A. J. Sub-Bandgap Photocurrent Spectra of p-i-n Perovskite Solar Cells with n-Doped Fullerene Electron Transport Layers and Bias Illumination. *ACS Appl. Energy Mater.* **2024**, *7* (14), 5869−5878.
(61) Hahn, V.; Messer, T.; Bojanowski, N. M.; Curticean, E. R.; Wacker, I.; Schröder, R. R.; Blasco, E.; Wegener, M. Two-Step Absorption Instead of Two-Photon Absorption in 3D Nanoprinting. *Nat. Photonics* **2021**, *15* (12), 932−938.
(62) Patel, J. B.; Milot, R. L.; Wright, A. D.; Herz, L. M.; Johnston, M. B. Formation Dynamics of $CH_3NH_3PbI_3$ Perovskite Following Two-Step Layer Deposition. *J. Phys. Chem. Lett.* **2016**, *7* (1), 96−102.
(63) Oo, A. M.; Fan, P.; Zhang, X.; Yu, J. Efficiency Improvement of Planar Inverted Perovskite Solar Cells by Introducing Poly 9,9-Dioctyfluorene-Co-Benzothiazole into Polytriarylamine as Mixed Hole-Transport Layer. *Energy Technol.* **2020**, *8* (3), 1901042.
(64) *APEX, SAINT and SADABS*; Bruker AXS Inc., 2007.
(65) Sheldrick, G. M. *SHELXT*- Integrated Space-Group and Crystal-Structure Determination. *Acta Crystallogr., Sect. A* **2015**, *71* (1), 3−8.
(66) Sheldrick, G. M. Crystal Structure Refinement with *SHELXL*. *Acta Crystallogr. Sect. C* **2015**, *71* (1), 3−8.
(67) Dolomanov, O. V.; Bourhis, L. J.; Gildea, R. J.; Howard, J. A. K.; Puschmann, H. OLEX2: A Complete Structure Solution, Refinement and Analysis Program. *J. Appl. Crystallogr.* **2009**, *42* (2), 339−341.
(68) Toby, B. H.; Von Dreele, R. B. *GSAS-II*: The Genesis of a Modern Open-Source All Purpose Crystallography Software Package. *J. Appl. Crystallogr.* **2013**, *46* (2), 544−549.
(69) Hanifi, D. A.; Bronstein, N. D.; Koscher, B. A.; Nett, Z.; Swabeck, J. K.; Takano, K.; Schwartzberg, A. M.; Maserati, L.; Vandewal, K.; van de Burgt, Y.; Salleo, A.; Alivisatos, A. P. Redefining Near-Unity Luminescence in Quantum Dots with Photothermal Threshold Quantum Yield. *Science* **2019**, *363* (6432), 1199−1202.
(70) Endres, J.; Egger, D. A.; Kulbak, M.; Kerner, R. A.; Zhao, L.; Silver, S. H.; Hodes, G.; Rand, B. P.; Cahen, D.; Kronik, L.; Kahn, A. Valence and Conduction Band Densities of States of Metal Halide Perovskites: A Combined Experimental-Theoretical Study. *J. Phys. Chem. Lett.* **2016**, *7* (14), 2722−2729.
(71) van Setten, M. J.; Giantomassi, M.; Bousquet, E.; Verstraete, M. J.; Hamann, D. R.; Gonze, X.; Rignanese, G.-M. The PseudoDojo: Training and Grading a 85 Element Optimized Norm-Conserving Pseudopotential Table. *Comput. Phys. Commun.* **2018**, *226*, 39−54.
(72) Perdew, J. P.; Burke, K.; Ernzerhof, M. Generalized Gradient Approximation Made Simple. *Phys. Rev. Lett.* **1996**, *77* (18), 3865−3868.
(73) Godby, R. W.; Needs, R. J. Metal-Insulator Transition in Kohn-Sham Theory and Quasiparticle Theory. *Phys. Rev. Lett.* **1989**, *62* (10), 1169−1172.
(74) Kronik, L.; Neaton, J. B. Excited-State Properties of Molecular Solids from First Principles. *Annu. Rev. Phys. Chem.* **2016**, *67*, 587−616.
(75) Kresse, G.; Hafner, J. Ab Initio Molecular Dynamics for Liquid Metals. *Phys. Rev. B* **1993**, *47* (1), 558−561.
(76) Kresse, G.; Furthmüller, J. Efficient Iterative Schemes for Ab Initio Total-Energy Calculations Using a Plane-Wave Basis Set. *Phys. Rev. B* **1996**, *54* (16), 11169−11186.
(77) Kresse, G.; Joubert, D. From Ultrasoft Pseudopotentials to the Projector Augmented-Wave Method. *Phys. Rev. B* **1999**, *59* (3), 1758−1775.
(78) Blöchl, P. E. Projector Augmented-Wave Method. *Phys. Rev. B* **1994**, *50* (24), 17953−17979.
(79) Bučko, T.; Lebègue, S.; Hafner, J.; Ángyán, J. G. Improved Density Dependent Correction for the Description of London Dispersion Forces. *J. Chem. Theory Comput.* **2013**, *9* (10), 4293−4299.
(80) Bučko, T.; Lebègue, S.; Ángyán, J. G.; Hafner, J. Extending the Applicability of the Tkatchenko-Scheffler Dispersion Correction via Iterative Hirshfeld Partitioning. *J. Chem. Phys.* **2014**, *141* (3), 034114.
(81) Jinnouchi, R.; Lahnsteiner, J.; Karsai, F.; Kresse, G.; Bokdam, M. Phase Transitions of Hybrid Perovskites Simulated by Machine-Learning Force Fields Trained on the Fly with Bayesian Inference. *Phys. Rev. Lett.* **2019**, *122* (22), 225701.
(82) Bartók, A. P.; Payne, M. C.; Kondor, R.; Csányi, G. Gaussian Approximation Potentials: The Accuracy of Quantum Mechanics, without the Electrons. *Phys. Rev. Lett.* **2010**, *104* (13), 136403.
(83) Bartók, A. P.; Kondor, R.; Csányi, G. On Representing Chemical Environments. *Phys. Rev. B* **2013**, *87* (18), 184115.
(84) Thiemann, F. L.; O'Neill, N.; Kapil, V.; Michaelides, A.; Schran, C. Introduction to Machine Learning Potentials for Atomistic Simulations. *J. Phys.: Condens. Matter* **2025**, *37* (7), 073002.
(85) Schnedermann, C.; Liebel, M.; Kukura, P. Mode-Specificity of Vibrationally Coherent Internal Conversion in Rhodopsin during the Primary Visual Event. *J. Am. Chem. Soc.* **2015**, *137* (8), 2886−2891.
(86) ASTM Standard G173-03. *Standard Tables for Reference Solar Spectral Irradiances: Direct Normal and Hemispherical on 37° Tilted Surface*; ASTM International, 2020.
(87) Moore, L. A.; Smith, C. M. Fused Silica as an Optical Material [Invited]. *Opt. Mater. Express* **2022**, *12* (8), 3043−3059.

Downloaded from pubs.acs.org/acscii/article-pdf/doi/10.1021/acscentsci.6c01379/6918706/acscentsci.6c01379.pdf by STANFORD UNIV user on 13 November 2026

https://doi.org/10.1021/acscentsci.6c01379
ACS Cent. Sci. XXXX, XXX, XXX−XXX